A novel formation mechanism of sulfamic acid ~~NH$_2$SO$_3$H~~ and its enhancing effect on methanesulfonic acid-methylamine aerosol particle formation in agriculture-developed and coastal industrial areas

Hui Wang [a,‡], Shuqin Wei [a,‡], Jihuan Yang [a,], Yanlong Yang [a,], Rongrong Li [a], Rui Wang [a],

Chongqin Zhu [b,*], Tianlei Zhang [a,*], Changming Zhang [c]

[a] *Shaanxi Key Laboratory of Catalysis, School of Chemical & Environment Science, Shaanxi University of Technology, Hanzhong, Shaanxi 723001, P. R. China*
[b] *College of Chemistry, Key Laboratory of Theoretical & Computational Photochemistry of Ministry of Education, Beijing Normal University, Beijing 100190, China.*
[c] *School of Mechanical Engineering, Shaanxi University of Technology, Hanzhong, Shaanxi 723001, P. R. China*

Abstract

Sulfamic acid (SFA) significantly impacts atmospheric pollution and poses potential risks to human health. Although traditional source of SFA and its role on sulfuric acid-dimethylamine new particle formation (NPF) has received increasing attention, the formation mechanism of SFA from HNSO$_2$ hydrolysis with ~~CH$_3$SO$_3$H~~ methanesulfonic acid (MSA) and its enhancing effect on MSA-methylamine (MA) NPF ~~methanesulfonic acid-methylamine APF~~ has not been studied, which will limit the understanding for the source and loss of SFA in agriculture-developed and coastal industrial areas. Here, the gaseous and interfacial formation of SFA from HNSO$_2$ hydrolysis with MSA ~~CH$_3$SO$_3$H~~ was investigated using quantum chemical calculations and BOMD simulations. Furthermore, the role of SFA in MSA-MA ~~CH$_3$SO$_3$H-CH$_3$NH$_2$~~ system was assessed using the ACDC kinetic model. Our simulation results indicate that the gaseous SFA formation from the hydrolysis of HNSO$_2$ with MSA ~~CH$_3$SO$_3$H~~ can be competitive with that catalyzed by H$_2$O within an altitude of 5-15 km. At the air-water interface, two types of reactions, the ions forming mechanism and the proton exchange mechanism to form SFA$^-$ ~~NH$_2$SO$_3$~~$\cdots$H$_3$O$^+$ ion pair were observed on the timescale of picosecond. Considering the overall environment of sulfuric acid emission reduction, the present findings suggest that SFA may play a significant role in NPF and the growth of aerosol particle as *i*) SFA can directly participate in the formation of MSA-MA ~~CH$_3$SO$_3$H-CH$_3$NH$_2$~~ -based cluster and enhance the rate of NPF from these clusters by approximately 10^3 times at 278.15 K; and *ii*) the SFA$^-$ ~~NH$_2$SO$_3$~~ species at the air-water interface can attract gaseous molecules to the aqueous surface, and thus promote particle growth.

---

* Corresponding authors, Tel: +86-0916-2641083, Fax: +86-0916-2641083.
  E-mail: cqzhu@bnu.edu.cn (C. Q. Zhu), ztianlei88@l63.com (T. L. Zhang).
  ‡ These authors contributed equally to this work.

1 Introduction

As a well-studied nitrogen derivative of sulfuric acid (Rennebaum et al., 2024), sulfamic acid (SFA)~~(NH₂SO₃H)~~ was not only recognized as a potent aerosol and cloud nucleating agent (Xue et al., 2024; Zhang et al., 2023; Pszona et al., 2015; Li et al., 2018), but also can harm human health through atmospheric deposition into water bodies (Van Stempvoort et al., 2019). In agriculture-developed and industrial areas with high ammonia (NH_3) concentrations, such as the Yangtze River Delta in China (Yu et al., 2020), Indo-Gangetic Plains (Kuttippurath et al., 2020), Pakistan, Bangladesh (Warner et al., 2016), and the southern Italy (Tang et al., 2021), the atmospheric concentration of SFA estimated by theoretical method of CCSD(T)-F12/cc-pVDZ-F12//M06-2X/6-311++G(3df,3pd) (Li et al., 2018) was expected to reach up to 10^8 molecules·cm^{-3}~~the atmospheric concentration of NH₂SO₃H was expected to reach up to10⁸ molecules·cm⁻³~~, and thus lead to it becoming a significant air pollutant. So, the sources of SFA in the atmosphere has been focused by several groups~~So, the sources of NH₂SO₃H in the atmosphere have been well investigated~~ (Lovejoy and Hanson, 1996; Pszona et al., 2015; Li et al., 2018; Larson and Tao, 2001; Manonmani et al., 2020; Zhang et al., 2022). The traditional source of SFA~~NH₂SO₃H~~ was mainly taken from the ammonolysis of SO_3 (Lovejoy and Hanson, 1996; Larson and Tao, 2001; Li et al., 2018). Experimentally, the rate coefficient for the ammonolysis of SO_3 was detected to be 2.0×10^{-11} cm^3·molecules^{-1}·s^{-1} at 295 K (Lovejoy and Hanson, 1996), which was close to the value for the hydrolysis of SO_3 assisted by water molecule (10^{-11}-10^{-10} cm^3 molecule^{-1} s^{-1}) (Kim et al., 1998; Hirota et al., 1996; Shi et al., 1994; Kolb et al., 1994; Long et al., 2013; Long et al., 2023; Ding et al., 2023; Cheng et al., 2023; Wang et al., 2024)~~(Kim et al., 1998; Hirota et al., 1996; Shi et al., 1994)~~. Theoretically, the ammonolysis of SO_3 to produce SFA~~NH₂SO₃H~~ can be catalyzed by NH_3. In arid and heavily polluted regions with high NH_3 concentrations, the effective rate coefficient for the ammonolysis of SO_3 can be sufficiently rapid, making it competitive with the conventional loss pathway of SO_3 with water (Li et al., 2018).

In addition to the ammonolysis of SO_3, new sources of SFA~~NH₂SO₃H~~ formation have received increasing attention (Zhang et al., 2022; Manonmani et al., 2020, Li et al., 2018, Xue et al., 2024). The existence of $HNSO_2$ was proposed in the reaction between SO_3 and NH_3, and was regarded as the most stable for nine different isomers of $HNSO_2$, HONSO, HOSNO, HOS(O)N, $HSNO_2$,

62 HSONO, HON(O)S, HOOSN, and HOONS (Deng et al., 2016). Owing to its similarity with SO_3

63 and the potential role of SO_3 in the atmosphere, the hydrolysis of $HNSO_2$ to produce SFA~~NH_2SO_3H~~

64 formation has been focused by several groups (Zhang et al., 2022; Manonmani et al., 2020). As the

65 direct hydrolysis of $HNSO_2$ with a high energy barrier takes place hardly in the gas phase (Zhang

66 et al., 2022; Manonmani et al., 2020), the addition of a second water molecule (Manonmani et al.,

67 2020), formic acid and sulfuric acid (H_2SO_4, SA) (Zhang et al., 2022) have been proved to promote

68 the product of SFA~~NH_2SO_3H~~ through the hydrolysis of $HNSO_2$. It was noted that, with the global

69 reduction in the concentration of H_2SO_4 resulting from SO_2 emission restrictions, the contribution

70 of methanesulfonic acid (MSA) to aerosol nucleation has received the widespread attention of

71 scientists. As a major inorganic acidic air pollutant (Chen et al., 2020), the concentration of MSA

72 in the atmosphere was noted to be notably high across various regions, spanning from coastal to

73 continental, with levels found to be between 10% and 250% of those measured for SA (Shen et al.,

74 2019; Dawson et al., 2012; Bork et al., 2014; Shen et al., 2020; Berresheim et al., 2002; Hu et al.,

75 2023). However, to the best of our knowledge, the gaseous hydrolysis of $HNSO_2$ with MSA has not

76 yet been investigated, which will confine the understanding for the source of SFA in regions with

77 significant pollution and high levels of MSA. ~~However, to the best of our knowledge, the gaseous~~

78 ~~hydrolysis of $HNSO_2$ with CH_3SO_3H has not yet been investigated. It was noted that, with the global~~

79 ~~reduction in the concentration of H_2SO_4 resulting from SO_2 emission restrictions, the contribution~~

80 ~~of CH_3SO_3H to aerosol nucleation has received the widespread attention of scientists. As a major~~

81 ~~inorganic acidic air pollutant (Chen et al., 2020), the concentration of CH_3SO_3H in the atmosphere~~

82 ~~was noted to be notably high across various regions, spanning from coastal to continental, with~~

83 ~~levels found to be between 10% and 250% of those measured for SA (Shen et al., 2019; Dawson et~~

84 ~~al., 2012; Bork et al., 2014; Shen et al., 2020; Berresheim et al., 2002; Hu et al., 2023).~~ Thus,

85 understanding the hydrolysis of $HNSO_2$ with MSA~~CH_3SO_3H~~ in the gas phase was necessary for

86 exploring its impact on aerosols and human health.

87 $HNSO_2 + H_2O + $ MSA~~CH_3SO_3H~~ $\rightarrow$ SFA~~NH_2SO_3H~~ $+ $ MSA~~CH_3SO_3H~~ (1)

88 As a supplement to gas-phase reactions, interfacial reactions at the air-water interface not only

89 can accelerate the rates of atmospheric reactions but also may introduce new mechanisms (Freeling

90 et al., 2020; Zhong et al., 2019). For instance, the Criegee intermediates reacting with

91 MSA~~CH_3SO_3H~~ at the air-water interface can form the ion pair of $CH_3C(H)(OOH)(SO_3CH_3)$

3

92　　anhydride and H_3O^+ (Ma et al., 2020), which differs from the corresponding gaseous reaction where

93　　the MSA~~CH₃SO₃H~~ molecule acts solely as a reactant reacting with Criegee intermediates directly.

94　　As far as we know, $HNSO_2$ exhibit a significant interfacial preference, as the fact that the total

95　　duration time of $HNSO_2$ at the interface approximately accounts for 49.1% of the 150 ns simulation

96　　time (Fig. S1). However, the hydrolysis of $HNSO_2$ with MSA ~~CH₃SO₃H~~ has not been studied at the

97　　air-water interface, which will limit our understanding of how the hydrolysis of $HNSO_2$ with MSA

98　　differs in the gas phase and air-water interfaces.~~which will confine the understanding for the source~~

99　　~~of NH₂SO₃H in regions with significant pollution and high levels of CH₃SO₃H.~~

100　　From a structural point of view, two functional groups of $-NH_2$ and $-SO_3H$ in the

101　　SFA~~NH₂SO₃H~~ molecule can act as both hydrogen donors and acceptors to interact with atmospheric

102　　species. Previous studies have demonstrated that SFA has a potential role in new particle formation

103　　(NPF), as it not only clusters efficiently with itself and SA (Lovejoy and Hanson, 1996), but also

104　　can promote the nucleation rate of NPF initiated from SA-DMA by a factor of two in dry and

105　　severely contaminated areas with NH_3 (Li et al., 2018). Due to the concentration of SA in the

106　　atmosphere has decreased significantly with the scenario of SO_2 emission control measures, MSA-

107　　driven NPF has attracted growing attention (Dawson et al., 2012; Nishino et al., 2014; Chen and

108　　Finlayson-Pitts, 2017; Chen et al., 2020; Shen et al., 2020). Initially, the binary nucleation of MSA

109　　with inorganic ammonia and organic amines in the atmosphere has been reported, where MA

110　　exhibits the strongest enhancing capability~~Initially, the binary nucleation of MSA with inorganic~~

111　　~~ammonia and organic amines in the atmosphere has been reported, where MA exhibits the strongest~~

112　　~~enhancing capability~~ (Chen et al., 2016; Chen and Finlayson-Pitts, 2017; Shen et al., 2019; Hu et

113　　al., 2023). Subsequently, some reported results suggested that the triadic MSA-MA-driven NPF can

114　　exhibit greater nucleation rates competed to the binary of MSA-driven (Zhang et al., 2022: Hu et

115　　al., 2023). For example, both formic acid (Zhang et al., 2022) and trifluoroacetic acid (Hu et al.,

116　　2023) exhibit an excellent catalytic influence on MSA-MA-driven NPF. However, the SFA

117　　involved in MSA-MA-driven NPF has not been investigated, which is worth important to

118　　investigate whether SFA can exhibit a similar enhancing effect in MSA-MA as observed in SA-

119　　DMA.

120　　Herein, this work studied the catalytic effect of SFA on $HNSO_2$ hydrolysis and MSA-MA

121　　nucleation particle formation. Specifically, quantum chemical calculations were used firstly to

4

assess the atmospheric processes of the gaseous hydrolysis of HNSO$_2$ with MSA~~CH$_3$SO$_3$H~~. Then,

the gaseous and interfacial mechanisms differences of the HNSO$_2$ hydrolysis with MSA were

investigated applying the Born-Oppenheimer Molecular Dynamic (BOMD) simulation method.

Finally, the atmospheric implications and mechanism of SFA in the MSA-MA-dominated NPF

process have been evaluated through density functional theory and the Atmospheric Clusters

Dynamic Code (ACDC) (McGrath et al., 2012; Hu et al., 2023; Zhao et al., 2020; Zhang et al., 2024;

Tsona Tchinda et al., 2022; Liu et al., 2020) models to evaluate the potential effect of SFA on

nucleation and NPF. This work will not only deepen our understanding of the source of SFA, but

also reveal significant implications for new particle formation and aerosol particle growth in MSA

polluted areas.

2 Methodology

2.1 Quantum Chemical Calculations

The gaseous hydrolysis of HNSO$_2$ with MSA~~CH$_3$SO$_3$H~~ was comprehensively studied through

quantum chemistry simulations. Optimization of all the species were carried out by using the method

of M06-2X with 6-311++G(2df,2pd) basis set (Zhao and Truhlar, 2008; Elm et al., 2012; Bork et al.,

2014). Vibrational frequencies were subsequently computed at the M06-2X/6-311++G(2df,2pd)

~~same~~ level to ensure the reality of all stationary point's frequencies and the presence of only one

imaginary frequency in transition states. It is noted that the calculated bond distances and bond

angles at the M06-2X/6-311++G(2df,2pd) level (Fig. S2) agree well with the available values (Fig.

S2) from the experiment and three different theoretical levels of M06-2X/6-311++G(3df,2pd),

M062X/6-311++G(3df,3pd) and M06-2X/aug-cc-pVTZ levels. Also, at the M06-2X/6-

311++G(2df,2pd) level, internal reaction coordinate (IRC) analyses were conducted to verify the

connection from the transition states to the corresponding products (or reactants). All calculations

regarding for geometries and frequency were conducted with the aid of the Gaussian 09 (Frisch,

2009) program. Furthermore, single point energies were performed at the CCSD(T)-F12/cc-pVDZ-

F12 (Kendall et al., 1992; Adler et al., 2007) level utilizing the ORCA (Neese, 2012) program,

based on the optimized geometries mentioned above. The CCSD(T)/aug-cc-pVDZ method was

chosen to calculate the relative energies as the fact that, compared with unsigned error (Table S1)

calculated at the CCSD(T)/CBS//M06-2X/6-311++G(2df,2pd) level, unsigned errors calculated at

151 CCSD(T)-F12/cc-pVDZ-F12//M06-2X/6-311++G(2df,2pd) was 0.71 kcal·mol^{-1}.

2.2 Rate coefficients calculations

153 The rate coefficients for the hydrolysis of HNSO$_2$ with MSA~~CH$_3$SO$_3$H~~ were calculated

154 through a two-step process. Initially, the high-pressure-limit (HPL) rate coefficients were computed

155 applying VRC-VTST methods within the Polyrate package (Chuang et al., 1999). It's worth noting

156 that the electronic structure method for VRC-TST calculations is based on Gaussian 09 program

157 using the M06-2X/6-311++G(2df,2pd). Meanwhile, two pivot points were selected (Bao et al., 2016;

158 Long et al., 2021; Georgievskii and Klippenstein, 2003; Meana-Pañeda et al., 2024) to produce a

159 single-faceted dividing surface for the HNSO$_2$ hydrolysis (shown in Part S1 in the Supplement).

160 Subsequently, on the basis of the HPL rate coefficients, the rate coefficients for the hydrolysis of

161 HNSO$_2$ with MSA~~CH$_3$SO$_3$H~~ were calculated within the temperature range of 212.6-320.0 K and

162 pressures applying the Master Equation Solver for Multi-Energy Well Reactions (MESMER)

163 program (Glowacki et al., 2012). The rate coefficients for the barrierless steps transitioning between

164 reactants and pre-reactive complexes were assessed applying the Inverse Laplace Transform (ILT)

165 method within MESMER calculations, while the step transitioning between pre-reactive complexes

166 and post-reactive complexes via transition states were evaluated using the RRKM theory (Mai et

167 al., 2018) in combination with the asymmetric Eckart model. The details of the rate coefficient for

168 the hydrolysis of HNSO$_2$ without and with X (X = H$_2$O and MSA~~CH$_3$SO$_3$H~~) were given in Part 1,

169 Table 1 and Table S4.

2.3 BOMD Simulations

171 BOMD simulations were conducted applying DFT implemented in CP2K program

172 (Vandevondele et al., 2005; Hutter et al., 2014). The exchange and correlation interactions were

173 addressed using the Becke-Lee-Yang-Parr (BLYP) functional (Becke, 1988; Lee et al., 1988),

174 while Grimme's dispersion was applied to address weak dispersion interaction (Grimme et al.,

175 2010). The Goedecker-Teter-Hutter (GTH) conservation pseudopotential (Goedecker et al.,

176 1996; Hartwigsen et al., 1998) combine with Gaussian DZVP basis set (Vandevondele and

177 Hutter, 2007) and an auxiliary plane wave basis set were used to represent core and valence

178 electrons. Energy cutoffs (Zhong et al., 2017; Zhong et al., 2018; Zhong et al., 2019) of 280 Ry

179 for the plane wave basis set and 40 Ry for the Gaussian basis set were applied. The gaseous

180 reactions were simulated in the NVT ensemble at 300 K, with $15 \times 15 \times 15$ Å^3 supercells and the

181 time step of 1 fs. To simulate the water microdroplet, the system containing 191 water molecules

182 (Zhong et al., 2017) was utilized in $35 \times 35 \times 35$ Å^3 supercells. This setup included HNSO$_2$ and

183 MSA~~CH$_3$SO$_3$H~~ along with the water drop. Prior to the interfacial simulation, a 10 ps relaxation

184 period in the BOMD simulation was used to equilibrate the water microdroplet system with 191

185 molecules.

2.4 ACDC kinetics simulation

187 The ACDC model (McGrath et al., 2012; Hu et al., 2023; Zhao et al., 2020; Zhang et al., 2024;

188 Tsona Tchinda et al., 2022; Liu et al., 2020) was utilized to simulate the $(MSA)_x(MA)_y(SFA)_z$ (0

189 $\leq y \leq x + z \leq 3$) cluster formation rates and explore the potential mechanisms, where the most

190 stable structure of $(SFA)_x(MSA)_y(MA)_z$ ($0 \leq z \leq x + y \leq 3$) clusters were searched with

191 ABCluster software (Zhang and Dolg, 2015) (The details in Part S1 of the Supplement).~~The ACDC~~

192 ~~model was utilized to simulate the $(MSA)_x(MA)_y(SFA)_z$ ($0 \leq y \leq x + z \leq 3$) cluster formation~~

193 ~~rates and explore the potential mechanisms.~~ This simulation encompasses a variety of

194 temperatures and monomer concentrations to capture the dynamics under different

195 environmental conditions. Thermodynamic parameters, obtained from quantum chemical

196 calculations executed at the M06-2X/6-311++G(2df,2pd) level, were used as inputs for the

197 ACDC model. Notably, many benchmark studies (Zhao et al., 2020; Zhang et al., 2024; Tsona

198 Tchinda et al., 2022; Liu et al., 2020) show that the M06-2X functional has good performance

199 compared to other common functionals for gaining the Gibbs free energies. For all the M06-2X

200 calculations with the 6-311++G(2df,2pd) basis set was used, as it is a good compromise between

201 accuracy and efficiency and does not yield significant errors in the thermal contribution to the free

202 energy compared to much larger basis sets such as 6-311++G(3df,3pd), with the differences of

203 relative ΔG less than 1.75 kcal·mol^{-1} (Table S7). The temporal progression of cluster

204 concentrations was determined by numerically integrating the birth-death equation, leveraging

205 MATLAB's ode15s solver for enhanced accuracy.

$$\frac{dc_i}{dt} = \frac{1}{2}\sum_{j<i}\beta_{j,(i-j)}c_jc_{(i-j)} + \sum_j\gamma_{(i+j)\to i}c_{i+j} - \sum_j\beta_{i,j}c_ic_j - \frac{1}{2}\sum_{j<i}\gamma_{i\to j}c_i + Q_i - S_i \qquad (2)$$

207 Here, c_i represents the concentration of a specific cluster, labelled as i; the term $\beta_{i,j}$ was used to

208 denote the collision coefficient, which was a measure of the frequency at which clusters i and j

209 collide with each other in a given environment or system; the coefficient $\gamma_{(i+j)\to i}$ was defined

7

210 as the evaporation rate constant that describes the process of a larger cluster, consisting of

211 combined elements i and j, breaking down into the individual smaller clusters i and j; and Q_i

212 encompasses all other source terms contributing to the formation of cluster i. S_i signifies

213 alternative sink terms for cluster i that may remove it from the system. Considering the

214 formation Gibbs free energy (Table S8) and evaporation rates (Table S9) of all clusters, the

215 clusters containing pure MSA and MA molecules as well as the clusters containing a SFA

216 molecule are mostly more stable and therefore are allowed to form larger clusters and contribute

217 to particle formation rates. In this case, clusters $(MSA)_4 \cdot (MA)_3$, $(MSA)_4 \cdot (MA)_4$ and

218 $SFA \cdot (MSA)_3 \cdot (MA)_3$ are set as the boundary clusters.

3. Results and discussions

3.1 The hydrolysis of $HNSO_2$ with MSA~~CH_3SO_3H~~ in the gas phase

221 Given the low chance of three molecules of $HNSO_2$, H_2O and MSA~~CH_3SO_3H~~ colliding

222 simultaneously under atmospheric conditions, the hydrolysis of $HNSO_2$ with MSA~~CH_3SO_3H~~

223 (Channel MSA) was likely a sequential bimolecular process. As the concentration of water molecule

224 (10^{18} molecules·cm^{-3} (Anglada et al., 2013)) in the atmosphere is much higher than those of $HNSO_2$

225 and MSA (10^5-10^9 molecules·cm^{-3} (Shen et al., 2020)), the reaction pathway of $HNSO_2 \cdots MSA +$

226 H_2O is hard to occur in actual atmospheric conditions. So, Channel MSA proceeds through the

227 initial formation of dimers ($HNSO_2 \cdots H_2O$ and $MSA \cdots H_2O$) via collisions between $HNSO_2$ (or

228 MSA) and H_2O. ~~As the concentration of water molecule (10^{18} molecules·cm^{-3}) in the atmosphere is~~

229 ~~much higher than those of $HNSO_2$ and CH_3SO_3H (10^5-10^9 molecules·cm^{-3}), the reaction pathway~~

230 ~~of $HNSO_2 \cdots CH_3SO_3H + H_2O$ is hard to occur in actual atmospheric conditions. So, Channel MSA~~

231 ~~proceeds through the initial formation of dimers ($HNSO_2 \cdots H_2O$ and $CH_3SO_3H \cdots H_2O$) via collisions~~

232 ~~between $HNSO_2$ (or CH_3SO_3H) and H_2O.~~ Subsequently, the generated dimer interacts with the third

233 reactant, either MSA~~CH_3SO_3H~~ or $HNSO_2$. As seen in Fig. 1, the calculated Gibbs free energy of

234 MSA~~CH_3SO_3H~~$\cdots H_2O$ complex was -0.9 kcal·mol^{-1}, which was 4.5 kcal·mol^{-1} lower than that of

235 $HNSO_2 \cdots H_2O$. Consequently, it was predicted the primary route for the hydrolysis reaction of

236 $HNSO_2$ with MSA~~CH_3SO_3H~~ takes place via the $HNSO_2 +$ MSA~~CH_3SO_3H~~$\cdots H_2O$ reaction.

237 Starting from the $HNSO_2 +$ MSA~~CH_3SO_3H~~$\cdots H_2O$ reactants, the Channel MSA was initiated

238 through the intermediate complex designated as IM_MSA1. From a geometric perspective,

239   IM_MSA1 complex exhibits a cage-like configuration by a van der Waals force (S1···O1, 2.00 Å)

240   and the involvement of three hydrogen bonds of H2···O4 (1.53 Å), H4···N1 (1.60 Å) and H5···O3

241   (2.07 Å). The Gibbs free energy of IM_MSA1 complex relative to $HNSO_2$ + MSA~~CH_3SO_3H~~···H_2O

242   reactants was 1.7 kcal·mol^{-1}. Subsequently, as presented in Fig. 1, Channel MSA progresses through

243   transition state TS_MSA1 to yield complex IMF_MSA1. At TS_MSA1, the MSA~~CH_3SO_3H~~ moiety

244   facilitates two hydrogen atom transfer, with TS_MSA1 lying only 0.8 kcal·mol^{-1} above complex

245   IM_MSA1. Complex IMF_MSA1 exhibits a cage-like structure with a Gibbs free energy was 23.4

246   kcal·mol^{-1} lower than that of IM_MSA1, revealing thermodynamic favorability of $HNSO_2$

247   hydrolysis with MSA~~CH_3SO_3H~~. To evaluate the relative catalytic impact of MSA~~CH_3SO_3H~~ and

248   H_2O, Fig. S4 illustrates the profiles of Gibbs free energy for the hydrolysis of $HNSO_2$ and the

249   corresponding reaction assisted by H_2O. Compared to complex $HNSO_2$···$(H_2O)_2$, the Gibbs

250   stabilization energy of IM_MSA1 increased by 5.6 kcal·mol^{-1}, potentially shortening the S1···O1

251   bond distance by 0.21 Å. Considering the Gibbs free energy barrier and rate coefficients,

252   MSA~~CH_3SO_3H~~ demonstrates a greater catalytic role compared to H_2O in lowering the energy

253   barrier for the hydrolysis of $HNSO_2$. In particular, MSA~~CH_3SO_3H~~ facilitates hydrogen atom to

254   extraction from H_2O, further reducing the reaction energy barriers to 7.7 kcal·mol^{-1}. Meanwhile, the

255   calculated rate coefficients for $HNSO_2$ hydrolysis with MSA~~CH_3SO_3H~~ was 3.08×10^{-11}-3.50×10^{-11}

256   cm^3·molecule^{-1}·s^{-1} within 212.6-320.0 K, exceeding corresponding values for reactions involving

257   H_2O by 2 orders of magnitude. Besides, the Gibbs free energy of IMF_MSA1 was 2.0 kcal·mol^{-1}

258   lower than that of the product complex IMF_WM1 (SFA~~NH_2SO_3H~~ ···H_2O), suggesting

259   SFA~~NH_2SO_3H~~ has a higher affinity for MSA~~CH_3SO_3H~~MSA~~CH_3SO_3H~~ compared to H_2O. Besides,

260   MSA-assisted $HNSO_2$ hydrolysis is reduced by 4.9 kcal·mol^{-1} in energy barrier than the NH_3-

261   assisted ammonolysis of SO_3 with its rate constant at 298 K (2.85×10^{-11} cm^3·molecule^{-1}·s^{-1}) close

262   to the value of ammonolysis of SO_3 with NH_3 (4.35×10^{-10} cm^3·molecule^{-1}·s^{-1}) (Li et al., 2018).

263   However, due to the absence of the concentration of $HNSO_2$, the competitiveness of these two

264   reactions cannot be further confirmed.~~Besides, CH_3SO_3H-assisted $HNSO_2$ hydrolysis is reduced by~~

265   ~~4.9 kcal·mol^{-1} in energy barrier than the NH_3-assisted ammonolysis of SO_3 with their rate constants~~

266   ~~close each other (4.35×10^{-10} cm^3·molecule^{-1}·s^{-1}) (Li et al., 2018). As the absence of the~~

267   ~~concentration of $HNSO_2$, the competitiveness of these two reactions cannot be further confirmed.~~

268   To evaluate the comparative catalytic ability of X (X = H_2O and MSA~~CH_3SO_3H~~) in the

269 atmosphere, the effective rate coefficients (k') for X-assisted $HNSO_2$ hydrolysis were calculated in

270 Table 1. Notably, k' serves as a metric for gauging the comparative catalytic ability of a series of

271 gaseous catalysts in atmospheric reactions (Sarkar et al., 2017; Zhang et al., 2020; Zhang et al.,

272 2019; Buszek et al., 2012; Gonzalez et al., 2011; Parandaman et al., 2018; Anglada et al., 2013).

273 When X was present, the calculated k' was given by Eq. (3).

274 $$k'_X = k_X \times K_{eq}(X \cdots H_2O) \times [X] \tag{3}$$

275 In Eq. (3), k_X was the rate coefficient for X-assisted $HNSO_2$ hydrolysis (Table 1), while $K_{eq}(X \cdots H_2O)$

276 denotes the equilibrium coefficients of $X \cdots H_2O$ (Table S2). [X] represents the avaiable

277 concentrations of H_2O (Anglada et al., 2013) and MSA~~CH_3SO_3H~~ (Shen et al., 2020). As indicated

278 in Table 1, at experimental concentrations ([H_2O] = 5.16×10^{16}-2.35×10^{18} molecules·cm^{-3}) within

279 280.0-320.0 K (at 0 km), the computed k'_{WM} ranged from 5.99×10^{-18}-7.79×10^{-17} cm^3·molecule^{-1}·s^{-1}.

280 $^{-1}$·s^{-1}. This range exceeded k'_{MSA} (4.60×10^{-21}-4.81×10^{-20} cm^3·molecule^{-1}·s^{-1}) by 2-4 orders of

281 magnitude, highlighting pronounced impact of H_2O compared to MSA~~CH_3SO_3H~~ at 0 km in

282 enhancing the rate of $HNSO_2$ hydrolysis. However, with the significant decrease in atmospheric

283 water molecules with increasing altitude, the calculated k'_{MSA} ranged from 1.96×10^{-19}·s^{-1}-$1.30 \times$

284 10^{-17}·cm^3·molecule^{-1}·s^{-1}, surpassing k'_{WM} (9.85×10^{-27}-6.51×10^{-22}·cm^3·molecule^{-1}·s^{-1}) by 3-10

285 orders of magnitude. This illustrates that MSA~~CH_3SO_3H~~ has a significantly greater catalytic ability

286 than H_2O in accelerating the rate of $HNSO_2$ hydrolysis within 5-15 km. So, $HNSO_2$ hydrolysis with

287 MSA~~CH_3SO_3H~~ may represent a potential formation pathway for MSA~~CH_3SO_3H~~ across an altitude

288 scope of 5-15 km.

289 **3.2 Reactions at the air-water interface**

290 The interfacial mechanism of MSA~~CH_3SO_3H~~-assisted $HNSO_2$ hydrolysis at the air-water

291 interface has not been thoroughly investigated. Interestingly, our simulations show that $HNSO_2$ and

292 MSA~~CH_3SO_3H~~molecules spend approximately 49.1% and 12.1% of the time, respectively, at the

293 air-water interface during the 150 ns simulation (Fig. S1 and Fig. S6). This reveals that the presence

294 of $HNSO_2$ and MSA~~CH_3SO_3H~~ at the air-water interface should not be disregarded. Therefore,

295 BOMD simulations were performed to clarify the interfacial mechanism of MSA~~CH_3SO_3H~~-assisted

296 $HNSO_2$ hydrolysis at the air-water interface. Comparable to the reactions of SO_3 at the air-water

297 interface with acidic molecules (Cheng et al., 2023; Zhong et al., 2019a), the hydrolysis of $HNSO_2$

298 with MSA~~CH_3SO_3H~~ at the air-water interface may occur through three pathways: (*i*) the adsorbed

299 ~~MSA~~CH$_3$SO$_3$H interacts with HNSO$_2$ at the air-water interface; (*ii*) the adsorbed HNSO$_2$ interacts

300 with MSA~~CH$_3$SO$_3$H~~ at the air-water interface; and (*iii*) the HNSO$_2$···MSA~~CH$_3$SO$_3$H~~ complex

301 reacts at the air-water interface. Nevertheless, because of the high reactiveness of MSA~~CH$_3$SO$_3$H~~

302 at the air-water interface, the lifetime of MSA~~CH$_3$SO$_3$H~~ was minimal (seen in Fig. S9) on the water

303 droplet, which was around a small number of picoseconds leading to the rapid formation of

304 MSA~~CH$_3$SO$_3$H$^-$~~ ion. Meanwhile, although HNSO$_2$ remains stable at the air-water interface (seen in

305 Fig. S8) and does not dissociate within 10 ps, the hydrated form of HNSO$_2$ illustrated in Fig. S8

306 was not conducive to HNSO$_2$ hydrolysis at the air-water interface. So, model (*iii*) was primarily

307 considered for HNSO$_2$ hydrolysis with MSA~~CH$_3$SO$_3$H~~ at the air-water interface. It was worth

308 noting that HNSO$_2$··· MSA~~CH$_3$SO$_3$H~~ complex can persist at the air-water interface for

309 approximately 34.2% of the 150 ns simulation time (see in Fig. S7). For model (*iii*), two types of

310 reactions were found at the air-water interface: (*a*) the NH$_2$SO$_3^-$ and H$_3$O$^+$ ions formation

311 mechanism, and (*b*) the proton exchange mechanism.

312   **NH$_2$SO$_3^-$ and H$_3$O$^+$ ions forming mechanism.** Fig. 2(a), Fig. S10 and Movie 1 illustrates the

313 formation mechanism of NH$_2$SO$_3^-$ and H$_3$O$^+$ ions through the chain structure. At 4.57 ps, a chain

314 hydrolyzed transition state was observed, accompanied by two protons transfer events. Specially,

315 an H2 atom transferred from the OH moiety of MSA~~CH$_3$SO$_3$H~~ molecule to the terminal N atom of

316 HNSO$_2$ molecule, resulting in the breaking of the O3-H2 bond (with the length of 1.49 Å) and

317 forming the H2-N bond (with the length of 1.14 Å). Concurrently, an interfacial water molecule

318 decomposes, leading to the elongation of the O1-H1 bond to over 1.00 Å, with the S1 atom of

319 HNSO$_2$ obtaining the OH moiety of the interfacial water molecule ($d_{(S1-O1)}$ = 1.60 Å). By 4.61 ps,

320 The N-H2 and S1-O1 bonds both shortened to 0.99 Å and 1.01 Å, revealing the formation of the

321 SFA~~NH$_2$SO$_3$H~~ molecule. However, due to its strong acidity, the SFA~~NH$_2$SO$_3$H~~ molecule could only

322 persist on the water droplet surface for a ps time-scale. As a result, at 7.43 ps, the proton of

323 SFA~~NH$_2$SO$_3$H~~ transferred to another interfacial water molecule, completing the deprotonation of

324 SFA~~NH$_2$SO$_3$H~~. The loop structure mechanism (Fig. 2(b), Fig. S11 and Movie 2) was similar with

325 the chain structure mechanism. However, in this case, the proton of SFA~~NH$_2$SO$_3$H~~ transferred to

326 CH$_3$SO$_3^-$ rather than to an interfacial water molecule.

327   **Proton exchange mechanism**. As depicted in Fig. 3, the proton exchange mechanism

328 illustrates the deprotonation of MSA~~CH$_3$SO$_3$H~~ concurrent with HNSO$_2$ hydration at the air-water

329   interface. As shown in Fig. 3(a), Fig. S12 and Movie 3, MSA~~CH₃SO₃H~~-mediated hydration HNSO₂

330   with a single water molecule was observed. Initially, the HNSO₂···MSA~~CH₃SO₃H~~ complex quickly

331   associates with an interfacial water molecule, and forms a loop structure complex that accelerates

332   the rate of proton transfer. By 4.38 ps, an eight-membered loop structure complex,

333   HNSO₂···H₂O···MSA~~CH₃SO₃H~~, emerges, characterized by two hydrogen bonds ($d_{(H2-N)} = 1.82$ Å

334   and $d_{(H1-O2)} = 1.92$ Å) and a van der Waals forces ($d_{(S1-O1)} = 2.35$ Å). Thereafter, at 4.77 ps, a

335   transition state-like configuration was identified where the water molecule within the loop complex

336   dissociated, elongating the O1-H1 bond to over 1.00 Å, and the S atom of HNSO₂ attaches to the

337   OH group of the interfacial water molecule. Concurrently, the $CH_3SO_3^-$ ion receives the proton from

338   the separated interfacial water molecule. The entire reaction for MSA~~CH₃SO₃H~~-mediated hydration

339   HNSO₂ with one water molecule was completed at 4.80 ps, resulting in the formation of

340   SFA~~NH₂SO₃H~~ and MSA~~CH₃SO₃H~~ molecules. MSA~~CH₃SO₃H~~-mediated hydration of HNSO₂ with

341   two water molecules (Fig. 3(b), Fig. S13 and Movie 4) at the air-water interface was similar with

342   mechanism identified with one water molecule. However, the inclusion of two water molecules

343   enlarges the loop, significantly reducing the stress on the loop structures. Consistent with the

344   prediction in Fig. 4, the loop structures preferred to include two water molecules rather than one

345   water molecule. This observation agrees well with the reported hydration of Criegee intermediate

346   at the air-water interface (Zhu et al., 2016; Kumar et al., 2018; Liu et al., 2021; Zhang et al., 2023a).

347   Additionally, MSA~~CH₃SO₃H~~-mediated hydration of HNSO₂ with three water molecules (Fig. S14

348   and Movie 5) has been observed in the proton exchange mechanism. However, its probability of

349   occurrence was smaller due to the relatively larger entropy effect. It was noteworthy that the

350   SFA~~NH₂SO₃H~~ and MSA~~CH₃SO₃H~~ molecules formed in the proton exchange mechanism were not

351   stable at the air-water interface, which can further interact with an interfacial water molecule to form

352   the corresponding ions of $NH_2SO_3^-$ and $CH_3SO_3^-$.

353   At the air-water interface, a sum of 50 BOMD trajectories, each lasting 10 ps, were conducted

354   to investigate HNSO₂ hydrolysis with MSA~~CH₃SO₃H~~. Two distinct mechanisms were observed:

355   the formation of $NH_2SO_3^-$ and H_3O^+ ions formation (shown in blue and yellow in Fig. 4) and the

356   proton exchange mechanism (represented by orange, purple and green in Fig. 4). In the mechanism

357   involving the formation of $NH_2SO_3^-$ and H_3O^+ ions, approximately 22% (Fig. 2(a), Fig. 4, Fig. S10

358   and Movie 1) of the reactions took place via a chain structure, while the majority (~18%) (Fig. 2(b),

359 Fig. 4, Fig. S11 and Movie 2) proceeded through a loop structure mechanism. This discrepancy can

360 be attributed to the uncertainty regarding the direction of proton transfer from SFA~~NH₂SO₃H~~. Since

361 the number of water molecules near the water microdroplet far exceeded that of $CH_3SO_3^-$, protons

362 were predominantly transferred to interface water molecules, making the loop structure mechanism

363 weaker than the chain structure mechanism. Approximately 60% of the reactions were observed to

364 be due to the proton exchange mechanism in BOMD simulations. Through water-mediated

365 mechanisms, these reactions resulted in SFA~~NH₂SO₃H~~ formation. Similarly to gas-phase reactions,

366 loop structures were observed in these reactions. Approximately 10% of the reactions formed a loop

367 structure involving one water molecule (Fig. 3(a), Fig. 4, Fig. S12 and Movie 3), while the most

368 common loop structure involved two water molecules (about 42%) (Fig. 3(b), Fig. 4, Fig. S13 and

369 Movie 4). Smaller loops were found to experience more stress than loop structures with two water

370 molecules. In cases of loop structures with three water molecules (about 8%) (Fig. 4, Fig. S14 and

371 Movie 5), the entropy effect was deemed to be more significant than the strain effect and likely

372 played a dominant role. The two water molecules contained in the loop structure not only acted as

373 a reactant but also facilitated proton transfer as a bridge.

374 **3.3 New Particle Formation from the atmospheric products**

375 **3.3.1. The influence of SFA on the stability of atmospheric MSA-MA-based**

376 **clusters**

377   Electrostatic Potential (ESP) mapping on the molecular van der Waals (vdW) surface was

378 employed to analyze the interactions between SFA and other key nucleation precursors like MSA

379 and MA. As shown in Fig. 5, sites with more negative ESP often attract more positive ESP sites,

380 namely hydrogen bonds in the studied system. Specifically, the hydrogen atoms of the -SO₃H and -

381 NH₂ groups (site 4 and 5) in SFA, possessing more positive ESP values, have the potential to attract

382 groups with negative ESP values, such as the oxygen atom within the -SO₃H group of MSA (site 6)

383 and the nitrogen atom of MA (site 1), thus forming hydrogen bonds as proton donors. Additionally,

384 the sulfur atom of the -SO₃H functional group (site 7) in SFA, with a negative ESP of -30.75, acts

385 as proton acceptor, facilitating direct binding with MSA and MA molecules via the hydrogen bonds.

386 Therefore, the introduction of SFA was believed to enhance the stability of MSA-MA clusters by

387 promoting the formation of more hydrogen bonds and facilitating proton transfers.

388 **3.3.2. The cluster formation rates in the SFA-MSA-MA system**

389   Simulations were conducted to determine the cluster formation rates (J) for the MSA-MA-SFA

390   system, varying parameters such as temperature and the concentrations of the precursors were

391   involved. To assess the promotional impact of SFA on J under varying atmospheric conditions, the

392   enhancement factor (R) was computed as the ratio of $J_{MSA-MA-SFA}$ to J_{MSA-MA}. As depicted in Fig. 6

393   (a), the J of MSA-MA-SFA system exhibits a negative correlation with temperature, attributed to

394   the decrease in ΔG value and evaporation rates of clusters at lower temperatures. Conversely, a

395   positive correlation of R with temperature was observed (Fig. 6(b)), indicating that SFA's

396   enhancement of nucleation was more pronounced in regions with relatively higher temperatures.

397   Furthermore, both J and R show an increase as the [SFA] increases, suggesting a positive correlation

398   of J and R with [SFA]. In short, in regions with high [SFA], such as the Yangtze River Delta of

399   China, Bangladesh, and the east coast of India, SFA was expected to significantly boost the J of

400   MSA-MA based nucleation. It is noted that in Fig. 6(b), due to the competitive relationship between

401   MSA and SFA, at low concentrations of SFA, the binding capacity of MSA with MA is stronger

402   than that of SFA with MA, resulting in only a small amount of SFA participating in cluster formation.

403   However, as the concentration of SFA increases, the number of $(MSA)_x \cdot (MA)_y \cdot (SFA)_z$ (where $y \leq$

404    $x + z \leq 3$) ternary clusters increase, leading to the formation of more hydrogen bonds and a

405   significant increase in R_{SFA}. Additionally, Fig. 7 illustrates the J and R of MSA-MA-SFA clusters

406   under different [MSA] and [MA]. On one hand, larger values of [MSA] and [MA] correspond to

407   higher J, as the increased concentration of nucleation precursors leads to a rise in the number of

408   MSA-MA-FSA clusters. On the other hand, increasing [MSA] and [MA] result in a decrease in the

409   R attributed to the effect of SFA on nucleation. This was because as [MSA] and [MA] increases,

410   the prevalence of pure MSA-MA clusters rise during the clustering process, consequently reducing

411   the impact of SFA.

3.3.3. The growth paths of cluster under different atmospheric conditions

413   Li et al. studied the atmospheric concentration of SFA estimated by theoretical method (Li et

414   al., 2018) was expected to reach up to10^8 molecules$\cdot$cm^{-3} in high NH$_3$ concentrations, such as

415   Yangtze River Delta in China (Yu et al., 2020), Indo-Gangetic Plains (Kuttippurath et al., 2020),

416   Pakistan, Bangla desh (Warner et al., 2016), and the southern Italy (Tang et al., 2021). Considering

417   the high-atmospheric concentrations of MSA and MA detected in coastal industrial areas (Stieger

418   et al., 2021; Mochizuki et al., 2017;), SFA could be an important contributor to MSA-MA-driven

NPF, such as the Yangtze River Delta in China, the east coast of India, the south of Bangladesh and Italy. To further evaluate the implication of SFA for the MSA-MA nucleation in the atmosphere, the growth paths of cluster was calculated under different atmospheric conditions. In Fig. 8 (a), two main types of cluster formation routes were found: (*i*) the pure MSA-MA pathway and (*ii*) the MSA-MA-SFA pathways at 278.15 K in the studied system. In the pure MSA-MA pathway, cluster growth primarily occurs through the collisional addition of MSA or MA monomers. Conversely, in the SFA-involved pathways, SFA can directly participate in the formation of stable larger clusters subsequently, such as $(MSA)_2 \cdot (MA)_2 \cdot SFA$ and $(MSA)_2 \cdot (MA)_2 \cdot (SFA)_2$ clusters, and then subsequently grow out. The involvement of SFA in the cluster formation pathway was significantly influenced by atmospheric conditions. Firstly, as the temperature rises from 238.15 K to 278.15 K, the contribution of the SFA-involved cluster formation pathways rises from 68% to 90% (Fig. 8 (b)), implying that the pathway involving SFA becomes increasingly important at lower altitudes or in warmer conditions. Secondly, as depicted in Fig. 8(c) and Fig. S22, the contribution of SFA to the MSA-MA system is primarily influenced by [SFA] and [MSA], with negligible dependence on [MA]. To assess the role of SFA in MSA-MA nucleation in the atmosphere, the specific contribution of the MSA-MA cluster growth paths at varying [SFA] to NPF was calculated at 278.15 K, as illustrated in Fig. 8(c), under the ambient conditions typical of the corresponding regions. Generally, as [SFA] increases from 10^4 to 10^8 molecules·cm^{-3}, the contribution of the SFA-involved pathway increases gradually. Specifically, at low [SFA] (10^4 molecules·cm^{-3}), the contributions of SFA-involved clustering pathways are 77% and 41% in regions with relatively low [MSA] in non-sea regions (Berresheim et al., 2002). In regions with high [SFA] (10^6, 10^8 molecules·cm^{-3}), the contributions of the SFA-MSA-MA growth pathways are dominant in their NPF. Particularly in areas with high [MSA], such as the Pacific Rim (6.26×10^8 molecules·cm^{-3} (Saltzman et al., 1986)), the central Mediterranean Sea (2.11×10^8 molecules·cm^{-3} (Mansour et al., 2020)) and the Amundsen Sea (3.65×10^9 molecules·cm^{-3} (Jung et al., 2020)), nucleation is primarily driven by the SFA-MSA-MA pathway, contributing to approximately 88% of cluster formation. These results suggest that the influence of SFA is more pronounced in regions with relatively high [MSA]. It is important to note that the [SFA] values discussed in this work are estimated from limited observational data based on the reaction between SO_3 and NH_3 in the atmosphere. Accurate determination of atmospheric [SFA] requires extensive field observations to enable more comprehensive research.

15

457 **3.4 Interfacial implications of products on aerosol particle growth**

458   As the discussion above, the formation of SFA$^-$···H$_3$O$^+$ and MSA$^-$···H$_3$O$^+$ ions pairs can occur

459 within a few picoseconds at the air-water interface. The atmospheric affinity of MSA$^-$, SFA$^-$ and

460 H$_3$O$^+$ for gaseous precursors was further probed by evaluating the free energies of interaction. It

461 was worth noting that compounds such as MSA, MA, HNO$_3$ (NA), and (COOH)$_2$ (OA) were

462 identified as candidate species for consideration (Wang et al., 2024; Kulmala et al., 2004). As

463 presented in Table 2, the computed binding energies demonstrate that the interactions of SFA$^-$

464 ···MSA, SFA$^-$···NA, SFA$^-$···OA, H$_3$O$^+$···MA, MSA$^-$···MSA, MSA$^-$···OA, and MSA$^-$···NA were

465 stronger than those of MSA···MA (one of the primary precursors for atmospheric aerosols), with

466 their Gibbs free energies increased by 14.3-50.9 kcal·mol^{-1}. The findings indicate that the presence

467 of SFA$^-$, MSA$^-$, and H$_3$O$^+$ at the interface facilitates the capture of potential gaseous species onto

468 the surface of water microdroplet.

469   Furthermore, we investigated the possibility of SFA$^-$ contributing to the enlargement of

470 particles within the MSA-MA cluster, taking into account the geometric configuration and the free

471 energy of formation for the (MSA)$_1$·(MA)$_1$·(SFA$^-$)$_1$ clusters aggregating. Compared with other

472 clusters, such as (MSA)$_1$·(MA)$_1$·(X)$_1$ (where X = HCOOH, CH$_3$COOH, CHOCOOH, OA,

473 CH$_3$COCOOH, HOOCCH$_2$COOH, HOOC(CH)$_2$COOH, HOOC(CH$_2$)$_2$COOH,

474 HOOC(CH$_2$)$_3$COOH, C$_6$H$_5$(COOH) and C$_{10}$H$_{16}$O$_3$) clusters (Zhang et al, 2022), the quantity of

475 hydrogen bonds within the (MSA)$_1$·(MA)$_1$·(SFA$^-$)$_1$ cluster has increased, and the loop of complex

476 was expanded. It has been demonstrated that SFA$^-$ has the greatest capacity to stabilize MSA-MA

477 clusters and facilitate MSA-MA nucleation in these clusters. This was attributed to its acidic nature

478 and structural characteristics, which include a greater number of intermolecular hydrogen bond

479   binding sites. Therefore, relative to $(MSA)_1 \cdot (MA)_1 \cdot (X)_1$ cluster (Table 2), the Gibbs formation free

480   energy ΔG of the $(MSA)_1 \cdot (MA)_1 \cdot (SFA^-)_1$ cluster was lower, indicating that the $NH_2SO_3^-$ ion

481   exhibits a more potent nucleation capacity at the air-water interface compared to the X species in

482   the gas phase. Consequently, our forecast was that the presence of $NH_2SO_3^-$ at the air-water interface

483   will foster enhanced particle growth.

4. Summary and Conclusions

485   In this study, quantum chemical calculations, BOMD simulations and ACDC kinetic model

486   were utilized to characterize the gaseous and interfacial hydrolysis of $HNSO_2$ with MSA~~CH_3SO_3H~~,

487   and to examine the influence exerted by SFA~~NH_2SO_3H~~ on MSA-MA-based clusters.

488   In the gaseous reaction, the activation energy for the hydrolysis of $HNSO_2$ catalyzed by

489   MSA~~CH_3SO_3H~~ was only 0.8 kcal·mol^{-1}, significantly lower by 7.7 kcal·mol^{-1} than the energy

490   barrier of H_2O-assisted $HNSO_2$ hydrolysis. The effective rate coefficients reveal that the

491   SFA~~NH_2SO_3H~~ formation from MSA~~CH_3SO_3H~~-catalyzed hydrolysis of $HNSO_2$ can be competitive

492   with that catalyzed by H_2O within an altitude of 5-15 km. Moreover, kinetic simulations utilizing

493   the ACDC have disclosed that SFA has an unexpectedly positive impact on the NPF process,

494   markedly enhancing the assembly of MSA-MA-based cluster. Notably, the "participant" mechanism

495   of SFA for cluster formation has been identified by tracing the growth paths of the system in

496   agriculture-developed and coastal industrial areas, especially significant in the Yangtze River Delta

497   of China, Bangladesh, and the east coast of India.

498   At the air-water interface, the $NH_2SO_3^-$ and H_3O^+ ions forming mechanism (~40%) and the

499   proton exchange mechanism (~60%) were observed in the hydrolysis of $HNSO_2$ with

500   MSA~~CH_3SO_3H~~, which can take place in a few picoseconds. Notably, the formed SFA~~NH_2SO_3H~~$^-$,

501   MSA~~CH_3SO_3H~~ $^-$, and H_3O^+ ions at the air-water interface possess the ability to attract potential

502   precursor molecules like MSA~~CH_3SO_3H~~, ~~CH_3NH_2~~MA, and HNO_3. This attraction facilitates the

503   transition of gaseous molecules onto the surface of water microdroplet. Moreover, the assessment

504   of the potential of X in the formation of the ternary MSA~~CH_3SO_3H~~-~~CH_3NH_2~~MA-X cluster

505   revealed that SFA~~NH_2SO_3~~$^-$ exhibits the greatest propensity to stabilize MSA~~CH_3SO_3H~~-~~CH_3NH_2~~

506   MA clusters and to foster nucleation of MSA~~CH_3SO_3H~~-~~CH_3NH_2~~-MA in the context of X.

507   Overall, this work not only elucidates a novel mechanism underlying the hydrolysis of $HNSO_2$

508 with MSA~~CH₃SO₃H~~, but also highlight the potential contribution of SFA on aerosol particle growth

509 and new particle formation.

Acknowledgments

Declaration of competing interest

515 The authors declare that they have no known competing financial interests or personal

516 relationships that could have appeared to influence the work reported in this paper.

Reference

Adler, T. B., Knizia, G., and Werner, H. J.: A simple and efficient CCSD(T)-F12 approximation, J. Chem. Phys., 127, 22, 2007.

Anglada, J. M., Hoffman, G. J., Slipchenko, L. V. M., Costa, M., Ruiz-Lopez, M. F., and Francisco, J. S.: Atmospheric significance of water clusters and ozone-water complexes, J. Phys. Chem. A, 117, 10381-10396, 2013.

Bao, J. L., Zhang, X., and Truhlar, D. G.: Barrierless association of CF_2 and dissociation of C_2F_4 by variational transition-state theory and system-specific quantum Rice-Ramsperger-Kassel theory, Proc. Natl. Acad. Sci. USA., 113, 13606-13611, 2016.

Becke, A. D.: Density-functional exchange-energy approximation with correct asymptotic behavior, Phys. Rev. A., 38, 3098-3100, 1988.

Berresheim, H., Elste, T., Tremmel, H. G., Allen, A. G., Hansson, H. C., Rosman, K., Dal Maso, M., Mäkelä, J. M., Kulmala, M., and O'Dowd, C. D.: Gas-aerosol relationships of H_2SO_4, MSA, and OH: Observations in the coastal marine boundary layer at Mace Head, Ireland, J. Geophys. Res. Atmos., 107, PAR 5-1-PAR 5-12, 2002.

Bork, N., Elm, J., Olenius, T., and Vehkamäki, H.: Methane sulfonic acid-enhanced formation of molecular clusters of sulfuric acid and dimethyl amine, Atmos. Chem. Phys., 14, 12023-12030, 2014.

Bork, N., Du, L., Reiman, H., Kurten, T., and Kjaergaard, H. G.: Benchmarking ab initio binding energies of hydrogen-bonded molecular clusters based on FTIR spectroscopy, J. Phys. Chem. A, 118, 5316-5322, 2014.

Buszek, R. J., Torrent-Sucarrat, M., Anglada, J. M., and Francisco, J. S.: Effects of a single water molecule on the OH + H_2O_2 reaction, J. Phys. Chem. A, 116, 5821-5829, 2012.

Chen, D., Li, D., Wang, C., Luo, Y., Liu, F., and Wang, W.: Atmospheric implications of hydration on the formation of methanesulfonic acid and methylamine clusters: A theoretical study, Chemosphere., 244, 125538-125547, 2020.

Chen, H. and Finlayson-Pitts, B. J.: New particle formation from methanesulfonic acid and amines/ammonia as a function of temperature, Environ. Sci. Technol., 51, 243-252, 2017.

Chen, H., Varner, M. E., Gerber., R. B., Finlayson-Pitts, B. J., Reactions of methanesulfonic acid with amines and ammonia as a source of new particles in air. J. Phys. Chem. B 2016, 120, 1526-1536.

Cheng, Y., Ding, C., Wang, H., Zhang, T., Wang, R., Muthiah, B., Xu, H., Zhang, Q., and Jiang, M.: Significant influence of water molecules on the SO_3 + HCl reaction in the gas phase and at the air-water interface, Phys. Chem. Chem. Phys., 25, 28885-28894, 2023.

Chuang, Y., Corchado, J., Fast, P., Villa, J., Coitino, E., Hu, W., Liu, Y., Lynch, G., Nguyen, K., and Jackels, C.: Polyrate-version 8.2, University of Minnesota, Minneapolis, 1999.

Dawson, M. L., Varner, M. E., Perraud, V., Ezell, M. J., Gerber, R. B., and Finlayson-Pitts, B. J.: Simplified mechanism for new particle formation from methanesulfonic acid, amines, and water via experiments and ab initio calculations, Proc. Natl. Acad. Sci. USA., 109, 18719-18724, 2012.

Dawson, M. L., Varner, M. E., Perraud, V. M., Ezell, M. J., Wilson, J. M., Zelenyuk, A., Gerber, R. B., and Finlayson-Pitts, B. J.: Amine-amine exchange in aminium-methanesulfonate aerosols, J. Phys. Chem. C., 118(50):29431-29440, 2014.

Deng, G., Wu, Z., Li, D., Linguerri, R., Francisco, J. S., and Zeng, X. J. J. o. t. A. C. S.: Simplest N-Sulfonylamine $HNSO_2$, J. Am. Chem. Soc, 140, 138, 11509-11512, 2016.

Ding, C., Cheng, Y., Wang, H., Yang, J., Li, Z., Lily, M., Wang, R., and Zhang, T.: Determination of the

influence of water on the SO_3 + CH_3OH reaction in the gas phase and at the air-water interface, Phys. Chem. Chem. Phys., 25, 15693-15701, 2023.

Elm, J.: Clusteromics II: methanesulfonic acid-base cluster formation, ACS omega., 6, 17035-17044, 2021.

Elm, J., Bilde, M., and Mikkelsen, K. V.: Assessment of density functional theory in predicting structures and free energies of reaction of atmospheric prenucleation clusters, J. Chem. Theory Comput., 8, 2071-2077, 2012.

Freeling, F., Scheurer, M., Sandholzer, A., Armbruster, D., Nödler, K., Schulz, M., Ternes, T. A., and Wick, A.: Under the radar – Exceptionally high environmental concentrations of the high production volume chemical sulfamic acid in the urban water cycle, Water Research., 175, 115706, 2020.

Frisch, M. J., Trucks, G. W., Schlegel, H. B., Scuseria, G. E., Robb, M. A., Cheeseman, J. R., Scalmani, G., Barone, V., Mennucci, B., Petersson, G. A., Nakatsuji, H., Caricato, M., Li, X., Hratchian, H. P., Izmaylov, A. F., Bloino, J., Zheng, G., Sonnenberg, J. L., Hada, M., Ehara, M., Toyota, K., Fukuda, R., Hasegawa, J., Ishida, M., Nakajima, T., Honda, Y., Kitao, O., Nakai, H., Vreven, T., Montgomery, J. A. Jr., Peralta, J. E., Ogliaro, F., Bearpark, M., Heyd, J. J., Brothers, E., Kudin, K. N., Staroverov, V. N., Kobayashi, R., Normand, J., Raghavachari, K., Rendell, A., Burant, J. C., Iyengar, S. S., Tomasi, J., Cossi, M., Rega, N., Millam, J. M., Klene, M., Knox, J. E., Cross, J. B., Bakken, V., Adamo, C., Jaramillo, J., Gomperts, R., Stratmann, R. E., Yazyev, O., Austin, A. J., Cammi, R., Pomelli, C., Ochterski, J. W., Martin, R. L., Morokuma, K., Zakrzewski, V. G., Voth, G. A., Salvador, P., Dannenberg, J. J., Dapprich, S., Daniels, A. D., Farkas, Ö., Foresman, J. B., Ortiz, J. V., Cioslowski, J., and Fox, D. J: Gaussian09 Revision D. 01, Gaussian Inc. Wallingford CT, Gaussian Inc. Wallingford CT, See also: URL: http://www. gaussian. com, 2009.

Georgievskii, Y. and Klippenstein, S.: Variable reaction coordinate transition state theory: analytic results and application to the C_2H_3+ H→ C_2H_4 reaction, JCP, 118, 5442-5455, 2003.

Glowacki, D. R., Liang, C.-H., Morley, C., Pilling, M. J., and Robertson, S. H.: MESMER: an open-source master equation solver for multi-energy well reactions, J. Phys. Chem. A, 116, 9545-9560, 2012.

Goedecker, S., Teter, M., and Hutter, J.: Separable dual-space Gaussian pseudopotentials, Phys. Rev. B., 54, 1703, 1996.

Gonzalez, J., Anglada, J. M., Buszek, R. J., and Francisco, J. S.: Impact of water on the OH + HOCl reaction, J. Am. Chem. Soc, 133, 3345-3353, 2011.

Grimme, S., Antony, J., Ehrlich, S., and Krieg, H.: A consistent and accurate ab initio parametrization of density functional dispersion correction (DFT-D) for the 94 elements H-Pu, J. Chem. Phys., 132, 154104, 2010.

Hartwigsen, C., Gœdecker, S., and Hutter, J.: Relativistic separable dual-space Gaussian pseudopotentials from H to Rn, Phys. Rev. B., 58, 3641-3662, 1998.

Hirota, K., Mäkelä, J., and Tokunaga, O.: Reactions of sulfur dioxide with ammonia: Dependence on oxygen and nitric oxide, Ind. Eng. Chem. Res., 35, 3362-3368, 1996.

Hu, Y., Chen, S., Ye, S., Wei, S., Chu, B., Wang, R., Li, H., and Zhang, T.: The role of trifluoroacetic acid in new particle formation from methanesulfonic acid-methylamine, Atmos. Environ., 311, 120001, 2023.

Hutter, J., Iannuzzi, M., Schiffmann, F., and VandeVondele, J.: Cp2k: atomistic simulations of condensed matter systems, WIRES COMPUT MOL SCI., 4, 15-25, 2014.

Jung, J., Hong, S. B., Chen, M., Hur, J., Jiao, L., Lee, Y., Park, K., Hahm, D., Choi, J. O., Yang, E. J., and Physics: Characteristics of methanesulfonic acid, non-sea-salt sulfate and organic carbon aerosols over the Amundsen Sea, Antarctica, Atmos. Chem. Phys., 20, 5405-5424, 2020.

Kendall, R. A., T. H. D., and Harrison, R. J.: Electron affinities of the first-row atoms revisited. Systematic basis sets and wave functions, J. Chem. Phys., 96, 6796-6806, 1992.

Kim, T. O., Ishida, T., Adachi, M., Okuyama, K., and Seinfeld, J. H.: Nanometer-sized particle formation from $NH_3/SO_2/H_2O$/air mixtures by ionizing irradiation, Aerosol Sci. Tech., 29, 111-125, 1998.

Kolb, C., Jayne, J., Worsnop, D., Molina, M., Meads, R., and Viggiano, A.: Gas phase reaction of sulfur trioxide with water vapor, J. Am. Chem. Soc., 116, 10314-10315, 1994.

Kulmala, M., Vehkamäki, H., Petäjä, T., Dal Maso, M., Lauri, A., Kerminen, V. M., Birmili, W., and McMurry, P. H.: Formation and growth rates of ultrafine atmospheric particles: a review of observations, J. Aerosol Sci., 35, 143-176, 2004.

Kumar, M., Li, H., Zhang, X., Zeng, X. C., and Francisco, J. S.: Nitric acid-amine chemistry in the gas phase and at the air-water interface, J. Am. Chem. Soc., 140, 6456-6466, 2018.

Kuttippurath, J., Singh, A., Dash, S., Mallick, N., Clerbaux, C., Van Damme, M., Clarisse, L., Coheur, P.-F., Raj, S., and Abbhishek, K.: Record high levels of atmospheric ammonia over India: Spatial and temporal analyses, Sci. Total Environ., 740, 139986, 2020.

Larson, L. J. and Tao, F.-M.: Interactions and reactions of sulfur trioxide, water, and ammonia: An ab initio and density functional theory study, J. Phys. Chem. A, 105, 4344-4350, 2001.

Lee, C., Yang, W., and Parr, R. G.: Development of the colle-Salvetti correlation-energy formula into a functional of the electron density, PHYS REV B, 37, 785, 1988.

Li, H., Zhong, J., Vehkamäki, H., Kurtén, T., Wang, W., Ge, M., Zhang, S., Li, Z., Zhang, X., Francisco, J. S., and Zeng, X. C.: Self-Catalytic reaction of SO_3 and NH_3 to produce sulfamic acid and its implication to atmospheric particle formation, J. Am. Chem. Soc, 140, 11020-11028, 2018.

Liu, J., Liu, Y., Yang, J., Zeng, X. C., and He, X.: Directional proton transfer in the reaction of the simplest criegee intermediate with water involving the formation of transient H_3O^+, J. Phys. Chem. Lett., 12, 3379-3386, https://doi.org/10.1021/acs.jpclett.1c00448, 2021.

Liu, L., Yu, F., Tu, K., Yang, Z., and Zhang, X.: Influence of atmospheric conditions on the role of trifluoroacetic acid in atmospheric sulfuric acid-dimethylamine nucleation, Atmos. Chem. Phys., 21, 6221-6230, 2021.

Long, B., Chang, C.-R., Long, Z.-W., Wang, Y.-B., Tan, X.-F., and Zhang, W.-J.: Nitric acid catalyzed hydrolysis of SO_3 in the formation of sulfuric acid: a theoretical study, Chem. Phys. Lett., 581, 26-29, 2013

Long, B., Wang, Y., Xia, Y., He, X., Bao, J. L., and Truhlar, D. G.: Atmospheric Kinetics: Bimolecular Reactions of Carbonyl Oxide by a Triple-Level Strategy, J. Am. Chem. Soc., 143, 8402-8413, 2021.

Long, B., Xia, Y., Zhang, Y.-Q., and Truhlar, D. G.: Kinetics of sulfur trioxide reaction with water vapor to form atmospheric sulfuric acid, J. Am. Chem. Soc., 145, 19866-19876, 2023.

Lovejoy, E. R. and Hanson, D. R.: Kinetics and products of the reaction $SO_3 + NH_3 + N_2$, J. Phys. Chem., 100, 4459-4465, 1996.

Ma, X., Zhao, X., Huang, Z., Wang, J., Lv, G., Xu, F., Zhang, Q., and Wang, W.: Determination of reactions between Criegee intermediates and methanesulfonic acid at the gas-liquid interface, Sci. Total Environ., 707, 135804, 2020.

Mai, T. V. T., Duong, M. V., Nguyen, H. T., and Huynh, L. K.: Ab initio kinetics of the $HOSO_2 + {}^3O_2 \rightarrow SO_3 + HO_2$ reaction, Phys. Chem. Chem. Phys., 20, 6677-6687, 2018.

Manonmani, G., Sandhiya, L., and Senthilkumar, K. J. I. J. O. Q. C.: Hydrolysis of $HNSO_2$: A potential route for atmospheric production of H_2SO_4 and NH_3, Int. J. Quantum Chem., 120, e26182, 2020.

Mansour, K., Decesari, S., Bellacicco, M., Marullo, S., Santoleri, R., Bonasoni, P., Facchini, M. C.,

648 Ovadnevaite, J., Ceburnis, D., and O'Dowd, C.: Particulate methanesulfonic acid over the central
649 Mediterranean Sea: source region identification and relationship with phytoplankton activity, Atmos.
650 Res., 237, 104837, 2020.

651 McGrath, M.J., Olenius, T., Ortega, I.K., Loukonen, V., Paasonen, P., Kurtén, T., Kulmala, M.,
652 Vehkamäki, H., Atmospheric cluster dynamics code: a flexible method for solution of the birth-death
653 equations. Atmos. Chem. Phys. 12, 2345-2355, 2012.

654 Meana-Pañeda, R., Zheng, J., Bao, J. L., Zhang, S., Lynch, B. J., Corchado, J. C., Chuang, Y.-Y., Fast, P.
655 L., Hu, W.-P., and Liu, Y.-P.: Polyrate 2023: A computer program for the calculation of chemical reaction
656 rates for polyatomics. New version announcement, Comput Phys Commun, 294, 108933, 2024.

657 Neese, F.: The ORCA program system, WIREs Comput. Mol. Sci., 2, 73-78, 2012.

658 Parandaman, A., Perez, J. E., and Sinha, A.: Atmospheric decomposition of trifluoromethanol catalyzed
659 by formic acid, J. Phys. Chem. A, 122, 9553-9562, 2018.

660 Pszona, M., Haupa, K., Bil, A., Mierzwicki, K., Szewczuk, Z., and Mielke, Z.: Clustering of sulfamic
661 acid: ESI MS and theoretical study, J. Mass Spectrom., 50, 127-135, 2015.

662 Rennebaum, T., van Gerven, D., Sebastian, S. S., and Wickleder, M. S.: Hydrazine sulfonic acid, NH_3NH
663 (SO_3), the bigger sibling of sulfamic acid, CHEM-EUR J, 30, e202302526, 2024.

664 Saltzman, E., Savoie, D., Prospero, J., and Zika, R.: Methanesulfonic acid and non-sea-salt sulfate in
665 Pacific air: Regional and seasonal variations,   J. Atmos. Chem., 4, 227-240, 1986.

666 Sarkar, S., Mallick, S., Kumar, P., and Bandyopadhyay, B.: Isomerization of methoxy radical in the
667 troposphere: Competition between acidic, neutral and basic catalysts, Phys. Chem. Chem. Phys., 19,
668 27848-27858, 2017.

669 Shang, D., Tang, L., Fang, X., Wang, L., Yang, S., Wu, Z., Chen, S., Li, X., Zeng, L., Guo, S., and Hu,
670 M.: Variations in source contributions of particle number concentration under long-term emission control
671 in winter of urban Beijing, Environ. Pollut., 304, 119072, 2022.

672 Shen, J., Elm, J., Xie, H.-B., Chen, J., Niu, J., and Vehkamaki, H.: Structural effects of amines in
673 enhancing methanesulfonic acid-driven new particle formation, Environ. Sci. Technol., 54, 13498-13508,
674 2020.

675 Shen, J., Xie, H.-B., Elm, J., Ma, F., Chen, J., and Vehkamaki, H.: Methanesulfonic acid-driven new
676 particle formation enhanced by monoethanolamine: A computational study, Environ. Sci. Technol., 53,
677 14387-14397, 2019.

678 Chen, H.; Varner, M. E.; Gerber, R. B.; Finlayson-Pitts, B. J.: Reactions of methanesulfonic acid with
679 amines and ammonia as a source of new particles in air, J. Phys. Chem. B, 120, 1526-1536, 2016.

680 Shi, Z., Ford, J., and Castleman Jr, A.: Cluster reactions of surlfur trioxide and ammonia, Chemical
681 physics letters, 220, 274-280, 1994.

682 Tang, Y. S., Flechard, C. R., Dämmgen, U., Vidic, S., Djuricic, V., Mitosinkova, M., Uggerud, H. T., Sanz,
683 M. J., Simmons, I., and Dragosits, U.: Pan-European rural monitoring network shows dominance of NH_3
684 gas and NH_4NO_3 aerosol in inorganic atmospheric pollution load, Atmos. Chem. Phys., 21, 875-914,
685 2021.

686 Tsona Tchinda, N., Du, L., Liu, L., and Zhang, X.: Pyruvic acid, an efficient catalyst in SO_3 hydrolysis
687 and effective clustering agent in sulfuric-acid-based new particle formation, Atmos. Chem. Phys., 22,
688 1951-1963, 2022.

689 Van Stempvoort, D., Spoelstra, J., Brown, S., Robertson, W., Post, R., and Smyth, S.: Sulfamate in
690 environmental waters, Sci. Total Environ., 695, 133734, 2019.

691 VandeVondele, J. and Hutter, J.: Gaussian basis sets for accurate calculations on molecular systems in

692   gas and condensed phases, J. Chem. Phys., 127, 114105, 2007.

693   VandeVondele, J., Krack, M., Mohamed, F., Parrinello, M., Chassaing, T., and Hutter, J.: Quickstep: Fast

694   and accurate density functional calculations using a mixed Gaussian and plane waves approach, Comput.

695   Phys. Commun., 167, 103-128, 2005.

696   Wang, R., Cheng, Y., Chen, S., Li, R., Hu, Y., Guo, X., Zhang, T., Song, F., and Li, H.: Reaction of SO_3

697   with H_2SO_4 and its implications for aerosol particle formation in the gas phase and at the air-water

698   interface, Atmos. Chem. Phys., 24, 4029-4046, 2024.

699   Wang, S., Nan, J., Shi, C., Fu, Q., Gao, S., Wang, D., Cui, H., Saiz-Lopez, A., and Zhou, B.: Atmospheric

700   ammonia and its impacts on regional air quality over the megacity of Shanghai, China, Sci. Rep, 5, 15842,

701   2015.

702   Warner, J. X., Wei, Z., Strow, L. L., Dickerson, R. R., Nowak, J. B., and Physics: The global tropospheric

703   ammonia distribution as seen in the 13-year AIRS measurement record, Atmos. Chem. Phys., 16, 5467-

704   5479, 2016.

705   Xue, J., Shao, X., Li, J., Li, J., Trabelsi, T., Francisco, J. S., and Zeng, X.: Observation of the Water-

706    $HNSO_2$ complex, J. Am. Chem. Soc., 146, 5455-5460, 2024.

707   Yu, X., Shen, L., Hou, X., Yuan, L., Pan, Y., An, J., and Yan, S.: High-resolution anthropogenic ammonia

708   emission inventory for the Yangtze River Delta, China, CHEMOSPHERE, 251, 126342, 2020.

709   Zhang, J. and Dolg, M.: AB Cluster: the artificial bee colony algorithm for cluster global optimization,

710   Phys. Chem. Chem. Phys., 17, 24173-24181, 2015.

711   Zhang, R., Khalizov, A., Wang, L., Hu, M., and Xu, W.: Nucleation and growth of nanoparticles in the

712   atmosphere, Chem. Rev., 112, 1957-2011, 2012.

713   Zhang, R., Shen, J., Xie, H. B., Chen, J., and Elm, J.: The role of organic acids in new particle formation

714   from methanesulfonic acid and methylamine, Atmos. Chem. Phys., 22, 2639-2650, 2022.

715   Zhang, T., Wen, M., Cao, X., Zhang, Y., Zeng, Z., Guo, X., Zhao, C., Lily, M., and Wang, R.: The

716   hydrolysis of NO_2 dimer in small clusters of sulfuric acid: A potential source of nitrous acid in

717   troposphere, Atmos. Environ., 243, 117876, 2020.

718   Zhang, T., Wen, M., Ding, C., Zhang, Y., Ma, X., Wang, Z., Lily, M., Liu, J., and Wang, R.: Multiple

719   evaluations of atmospheric behavior between Criegee intermediates and HCHO: Gas-phase and gas-

720   liquid interface reaction, J. Environ. Sci., 127, 308-319, 2023.

721   Zhang, T., Wen, M., Zhang, Y., Lan, X., Long, B., Wang, R., Yu, X., Zhao, C., and Wang, W.: Atmospheric

722   chemistry of the self-reaction of HO_2 radicals: stepwise mechanism versus one-step process in the

723   presence of $(H_2O)_n$ ($n = 1$-3) clusters, Phys. Chem. Chem. Phys., 21, 24042-24053, 2019.

724   Zhang, T., Zhang, Y., Tian, S., Zhou, M., Liu, D., Lin, L., Zhang, Q., Wang, R., and Muthiah, B.: Possible

725   atmospheric source of NH_2SO_3H: the hydrolysis of $HNSO_2$ in the presence of neutral, basic, and acidic

726   catalysts, Phys. Chem. Chem. Phys., 24, 4966-4977, 2022.

727   Zhang, X., Lian, Y., Tan, S., Yin, S., and Physics: Organ sulfate produced from consumption of SO_3

728   speeds up sulfuric acid-dimethylamine atmospheric nucleation, Atmos. Chem. Phys., 24, 3593-3612,

729   2024.

730   Zhang, Y., Wang, Z., Wang, H., Cheng, Y., Zhang, T., Ou, T., and Wang, R.: Atmospheric chemistry of

731   NH_2SO_3H in polluted areas: an unexpected isomerization of NH_2SO_3H in acid-polluted regions, J. Phys.

732   Chem. A, 127, 8935-8942, 2023.

733   Zhao, X., Shi, X., Ma, X., Zuo, C., Wang, H., Xu, F., Sun, Y., and Zhang, Q.: 2-Methyltetrol sulfate ester-

734   initiated nucleation mechanism enhanced by common nucleation precursors: A theory study, Sci. Total

735   Environ., 723, 137987, 2020.

736 Zhao, Y. and Truhlar, D. G.: The M06 suite of density functionals for main group thermochemistry,

737 thermochemical kinetics, noncovalent interactions, excited states, and transition elements: two new

738 functionals and systematic testing of four M06-class functionals and 12 other functionals, Theor. Chem.

739 Acc., 120, 215-241, 2008.

740 Zhong, J., Kumar, M., Francisco, J. S., and Zeng, X. C.: Insight into chemistry on cloud/aerosol water

741 surfaces, Acc. Chem. Res., 51, 1229-1237, 2018.

742 Zhong, J., Kumar, M., Zhu, C. Q., Francisco, J. S., and Zeng, X. C.: Frontispiece: surprising stability of

743 larger criegee intermediates on aqueous interfaces, ANGEW CHEM INT EDIT, 56, 7740-7744, 2017.

744 Zhong, J., Li, H., Kumar, M., Liu, J., Liu, L., Zhang, X., Zeng, X. C., and Francisco, J. S.: Mechanistic

745 insight into the reaction of organic acids with SO_3 at the air-water interface, ANGEW CHEM INT EDIT.,

746 131, 8351-8355, 2019.

747 Zhu, C., Kumar, M., Zhong, J., Li, L., Francisco, J. S., and Zeng, X. C.: New mechanistic pathways for

748 Criegee-water chemistry at the air/water interface, J. Am. Chem. Soc., 138, 11164-11169, 2016.
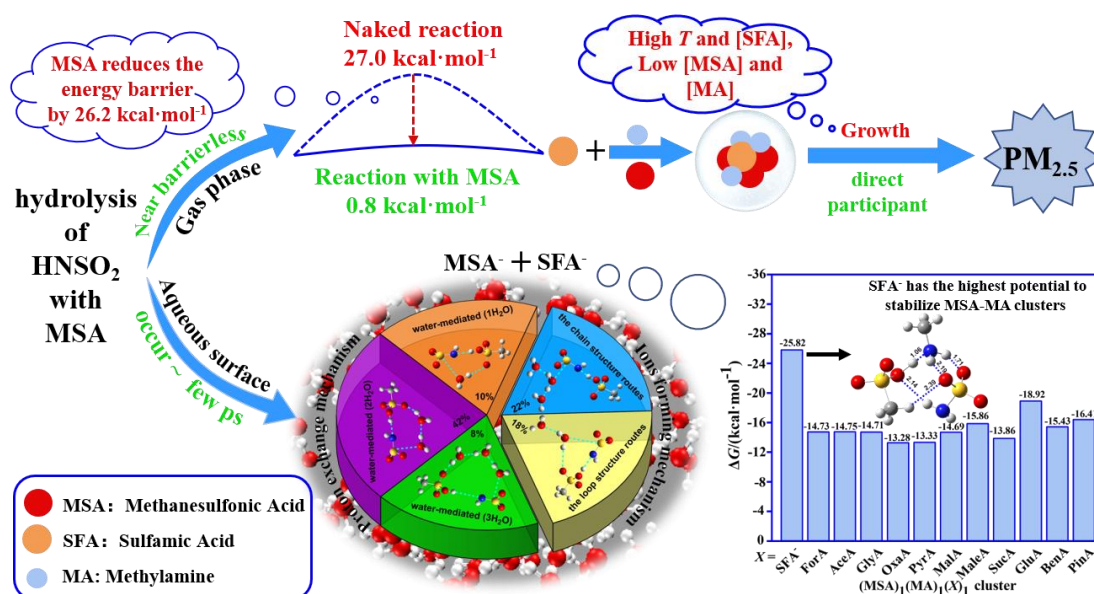
Graphical abstract

749

750

Figure Captions

752 **Fig. 1** The potential energy profile (ΔG) for the hydrolysis reaction of $HNSO_2$ with MSA at the

753 CCSD(T)-F12/cc-pVDZ-F12//M06-2X/6-311++G(2*df*,2*pd*) level of theory

754

755

756 **Fig. 2** BOMD simulation trajectories and snapshots of $NH_2SO_3^-$ and H_3O^+ ions forming mechanism

757 (chain structure (a) and loop-structure (b)) in the $HNSO_2$ hydrolysis with MSA at the air-water

758 interface

759

760

761 **Fig. 3** BOMD simulation trajectories and snapshots of proton exchange mechanism in MSA-

762 mediated hydration $HNSO_2$ with one (a) and two (b) water molecules at the air-water interface

763

764

765 **Fig. 4** Percentages of different mechanisms for the $HNSO_2$ hydrolysis with MSA at the air-water

766 interface observed in BOMD simulations

767

768

769 **Fig. 5** ESP-mapped molecular vdW surface of MA, SFA and MSA molecules at M06-2X/6-

770 311++G(2*df*,2*pd*) level of theory. Surface local minima and maxima of ESP of the different

771 functional groups in MA, SFA and MSA molecules are represented as blue and yellow spheres,

772 respectively. The values of maximum and minimum are shown in kcal mol^{-1} in the parentheses. The

773 green, red and blue arrows refer to the tendencies to form hydrogen bonds and proton transfer events,

774 respectively. (green = carbon, red = oxygen, blue = nitrogen, yellow = sulfur and white = hydrogen.)

775

776

777 **Fig. 6** The J (cm^{-3} s^{-1}) (a) and R (b) versus [SFA] with [MSA] = 10^6 molecules cm^{-3}, [MA] = 2.5 ×

778 10^8 molecules cm^{-3} and four different temperatures (green line: 298.15 K, blue line: 278.15 K, red

779 line: 258.15 K, black line: 238.15 K).

780

781

782 **Fig. 7** The J (cm^{-3} s^{-1}) (a) and R (b) as a function of [MSA] with [SFA] = 10^8 molecules cm^{-3} and

783 three different [MA] (black line: [MA] = 2.5 × 10^7 molecules cm^{-3}, red line: [MA] = 2.5 × 10^8

784 molecules cm^{-3}, blue line: [MA] = 2.5 × 10^9 molecules cm^{-3}) at 278.15 K.

785

786

787 **Fig. 8** Main cluster formation mechanism of MSA-MA-SFA-based system at 278.15 K, [MSA] =

788 10^7 molecules·cm^{-3}, [MA] = 2.5 × 10^8 molecules·cm^{-3}, and [SFA] = 10^6 molecules·cm^{-3}. (a) The

789 black arrows indicate the pure MSA-MA-based growth pathways. Blue arrows represent the

790 pathways containing SFA. The influence of (b) temperature, (c) [SFA] and [MSA] on the relative

791 contribution of the pure MSA-MA-based clustering pathway and the SFA participation pathway to

792 the system flux is analyzed. Others in (b), and (c) indicate that the pathway contribution of the

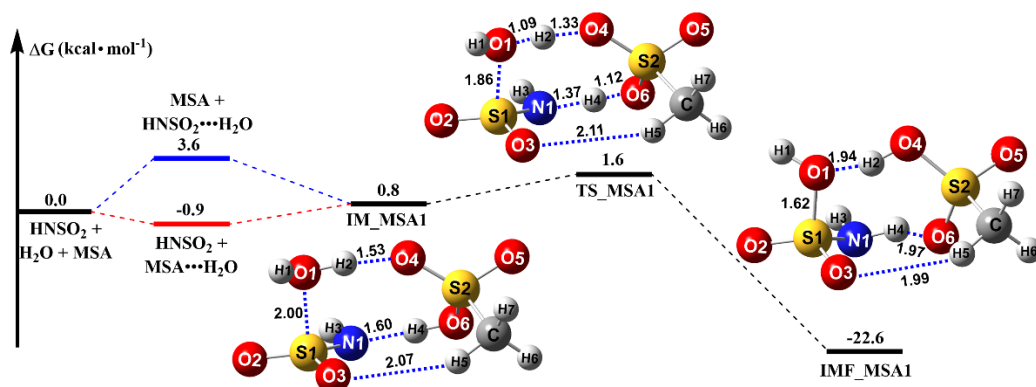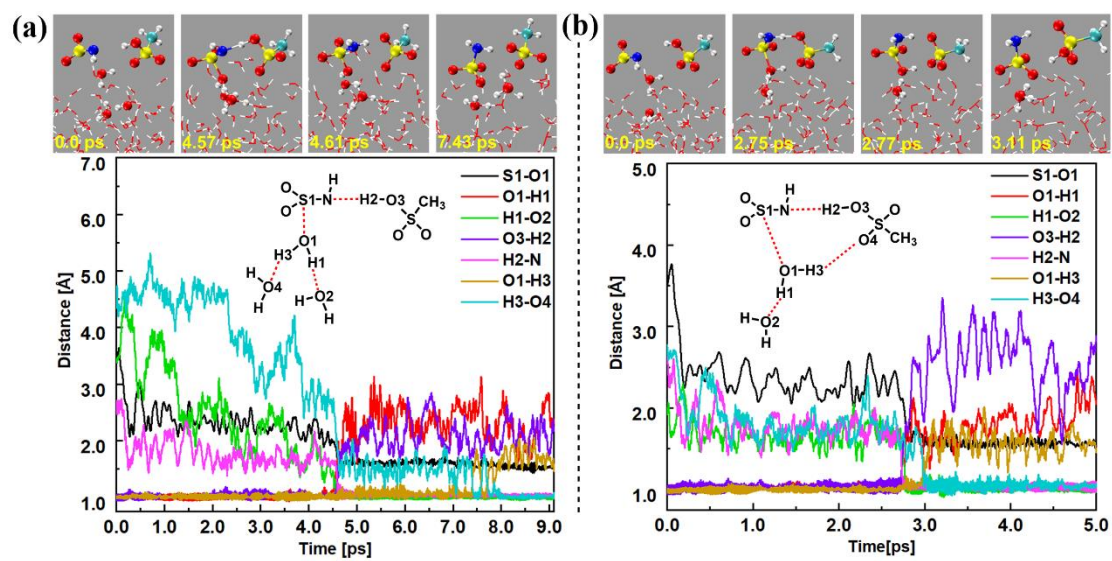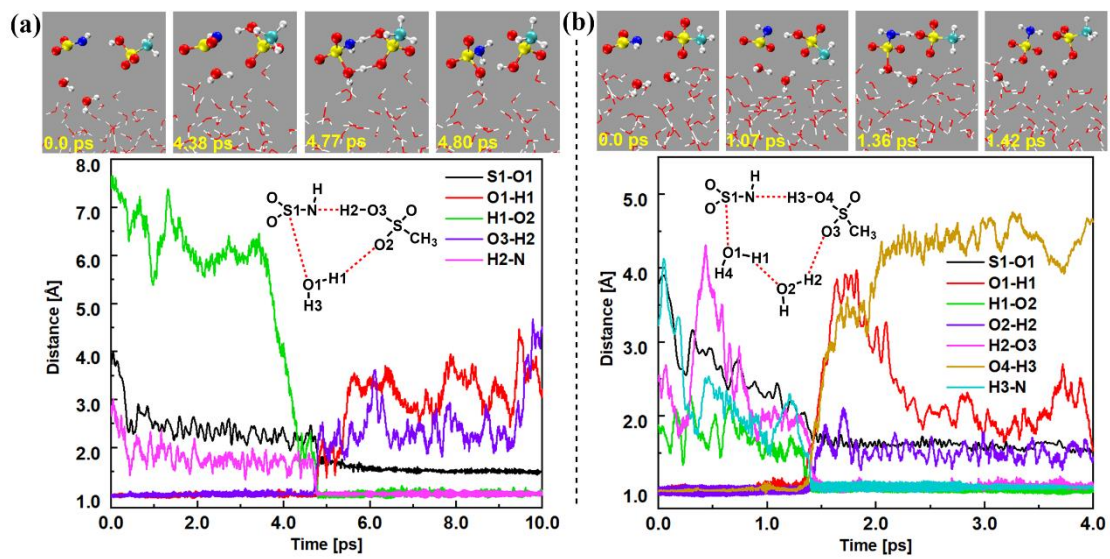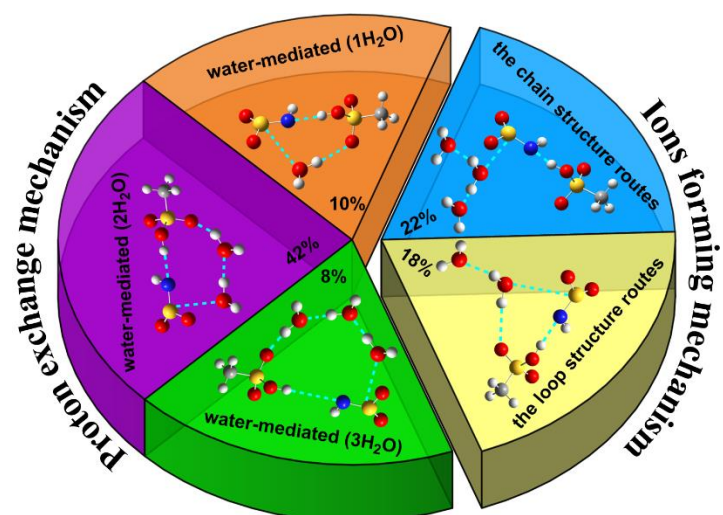793 cluster growing out of the studied system is less than 5%

Fig. 1

Fig. 2

798

799

800

Fig. 3

Fig. 4

Fig. 5

805
806   **Fig. 6**

(a)

[SFA] = 10^8, T = 278.15 K

Cluster formation rate J (cm^{-3} s^{-1})

- [MA] = 2.5×10^7 molecules·cm^{-3}
- [MA] = 2.5×10^8 molecules·cm^{-3}
- [MA] = 2.5×10^9 molecules·cm^{-3}

[MSA] (molecules·cm^{-3})

(b)

Enhancement strength R

[SFA] = 10^8 molecules·cm^{-3}, T = 278.15 K

- [MA] = 2.5×10^7 molecules·cm^{-3}
- [MA] = 2.5×10^8 molecules·cm^{-3}
- [MA] = 2.5×10^9 molecules·cm^{-3}

[MSA] (molecules·cm^{-3})

807
808

Fig. 7

33

Fig. 8

809
810
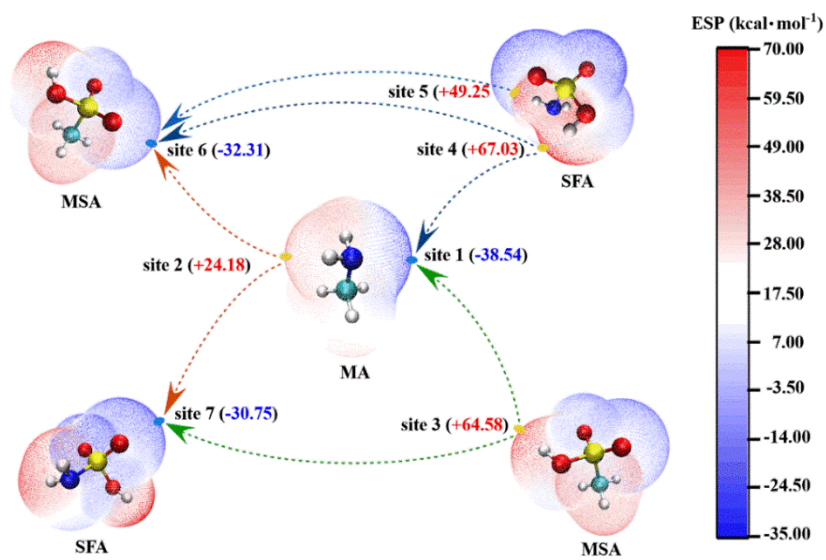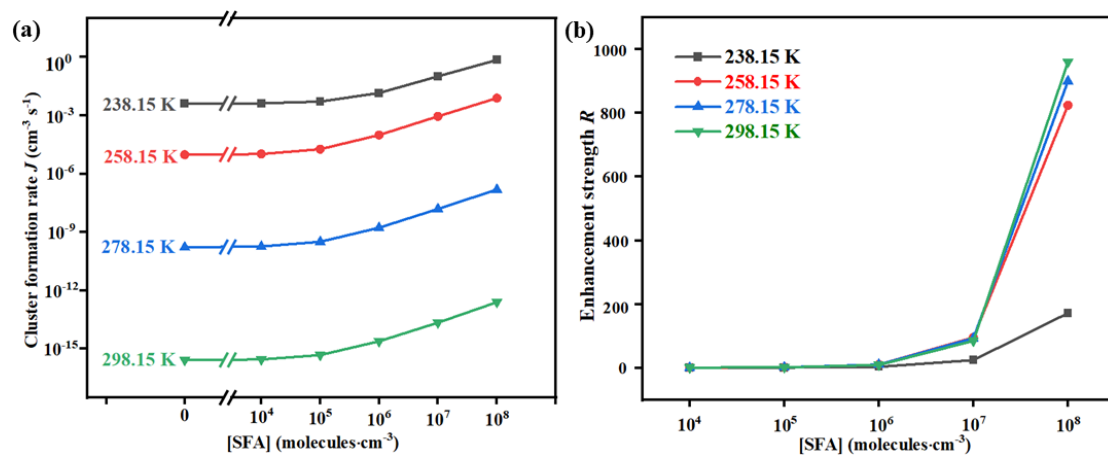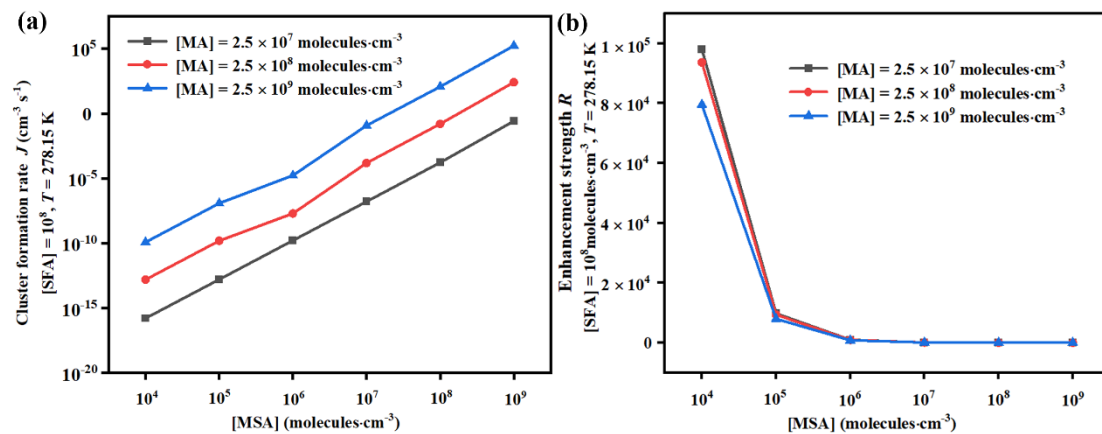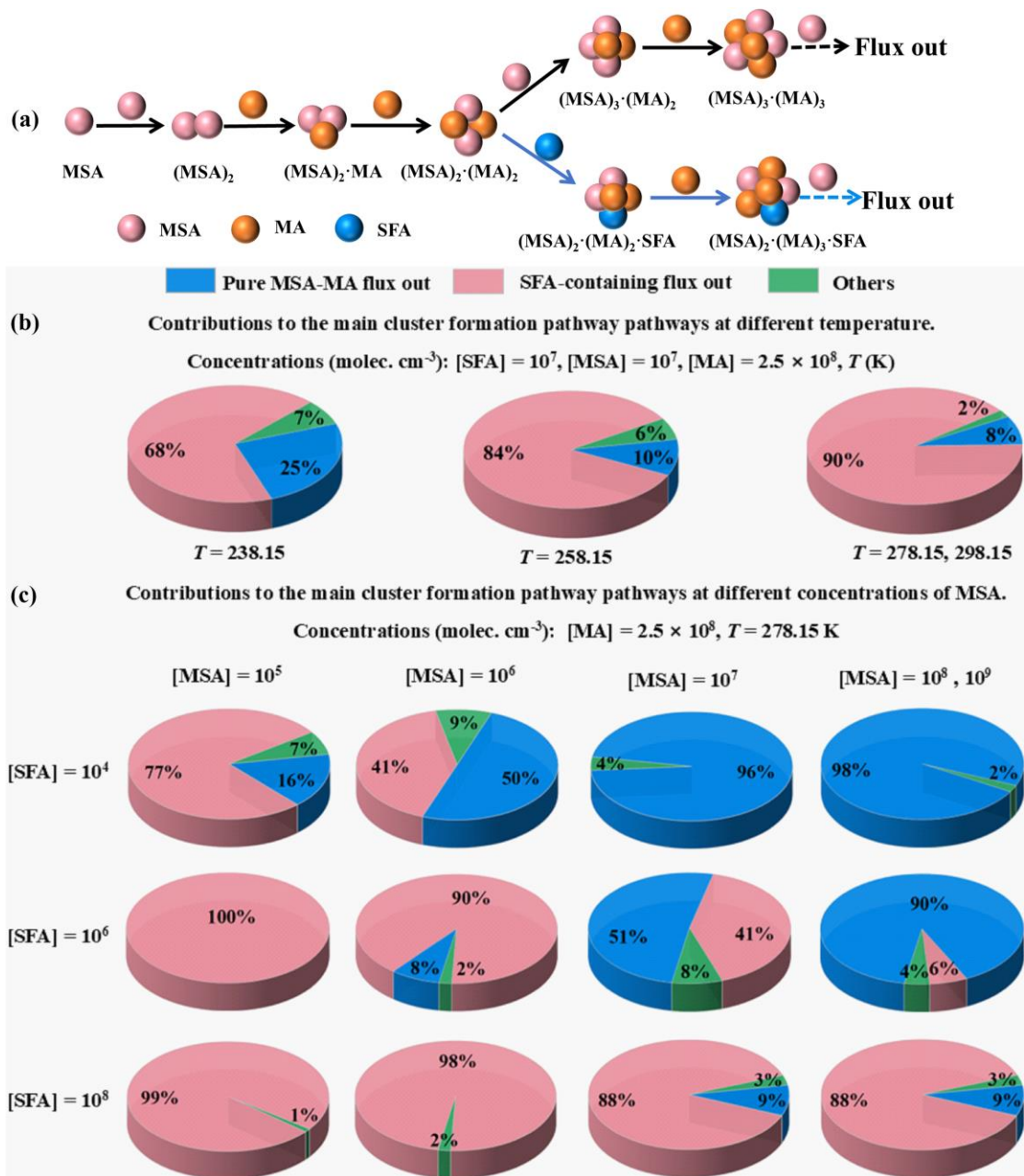
Table 1 Rate coefficients (k, cm^3·molecule^{-1}·s^{-1}) and effective rate constants (k', cm^3·molecule^{-1}·s^{-1}) for the hydrolysis of HNSO$_2$ with H$_2$O and MSA calculated by master equation within the temperature range of 213-320 K and altitude range of 0-15 km

Altitude		0 km						5 km	10 km	15 km
T/K		280	290	298	300	310	320	259.3	229.7	212.6
k_{WM}		7.64×10^{-13}	6.45×10^{-13}	5.63×10^{-13}	5.44×10^{-13}	4.59×10^{-13}	3.88×10^{-13}	1.09×10^{-12}	1.72×10^{-12}	2.22×10^{-12}
k_{MSA}		3.08×10^{-11}	2.96×10^{-11}	2.85×10^{-11}	2.82×10^{-11}	2.67×10^{-11}	2.52×10^{-11}	3.32×10^{-11}	3.49×10^{-11}	3.50×10^{-11}
k'_{WM}	20%RH	5.99×10^{-18}	7.96×10^{-18}	9.64×10^{-18}	1.03×10^{-17}	1.29×10^{-17}	1.36×10^{-17}			
	40%RH	1.19×10^{-17}	1.58×10^{-17}	1.99×10^{-17}	2.07×10^{-17}	2.60×10^{-17}	3.12×10^{-17}			
	60%RH	1.79×10^{-17}	2.38×10^{-17}	2.98×10^{-17}	3.11×10^{-17}	3.90×10^{-17}	4.68×10^{-17}	9.85×10^{-27}	1.71×10^{-22}	6.51×10^{-22}
	80%RH	2.39×10^{-17}	3.17×10^{-17}	3.97×10^{-17}	4.14×10^{-17}	5.21×10^{-17}	6.24×10^{-17}			
	100%RH	2.97×10^{-17}	3.96×10^{-17}	4.97×10^{-17}	5.18×10^{-17}	6.50×10^{-17}	7.79×10^{-17}			
k'_{MSA} [MSA]=10^8		4.81×10^{-19}	2.50×10^{-19}	1.57×10^{-19}	1.40×10^{-19}	7.90×10^{-20}	4.60×10^{-20}	1.96×10^{-20}	2.37×10^{-19}	1.30×10^{-18}
k'_{MSA}/k'_{WM}		1.62×10^{-4}	6.42×10^{-5}	3.16×10^{-5}	2.69×10^{-5}	1.22×10^{-5}	5.90×10^{-5}	3.01×10^{1}	1.38×10^{3}	1.32×10^{8}

k_{WM} and k_{MSA} are respectively the rate constant for the hydrolysis of HNSO$_2$ with H$_2$O and MSA; k'_{WM} and k'_{MSA} are respectively the effective rate constant for the hydrolysis of HNSO$_2$ with H$_2$O and MSA.

812 **Table 2.** Gibbs free energy (ΔG) for the formation of SFA$^-$···MSA, SFA$^-$···NA, SFA$^-$···OA,
813 H$_3$O$^+$···MA, MSA$^-$···MSA, MSA$^-$···OA, and MSA$^-$···NA, MSA···MA, (MSA)$_1$·(MA)$_1$·(X)$_1$ at 298
814 K

	SFA$^-$···MSA	SFA$^-$···HNO$_3$	SFA$^-$···OA	MSA$^-$···MSA	MSA$^-$···NA
ΔG	-23.8	-21.5	-25.2	-23.9	-22.6
	MSA$^-$··· OA	MSA···H$_3$O$^+$	MA···H$_3$O$^+$		MSA···MA
ΔG	-25.8	-35.8	-57.9		-7.0 (-7.2)[b]
	HCOOH ···MSA···MA	CH$_3$COOH ···MSA···MA	CHOCOOH ···MSA···MA		OA ···MSA···MA
ΔG	-14.7 (-15.8)[a]	-14.8 (-14.3)[a]	-14.7 (-15.6)[a]		-13.3 (-12.7)[a]
	CH$_3$COCOOH ···MSA···MA	HOOCCH$_2$COOH ···MSA···MA	HOOC(CH)$_2$COOH ···MSA···MA		HOOC(CH$_2$)$_2$COOH ···MSA···MA
ΔG	-13.3 (-13.0)[a]	-14.7 (-16.7)[a]	-15.9 (-15.3)[a]		-13.9 (-14.3)[a]
	HOOC(CH$_2$)$_3$COOH ···MSA···MA	C$_6$H$_5$(COOH) ···MSA···MA	C$_{10}$H$_{16}$O$_3$ ···MSA···MA		SFA$^-$ ···MSA···MA
ΔG	-18.9 (-17.9)[a]	-15.4 (-15.3)[a]	-16.4 (-15.3)[a]		-25.8

815 [a] The value was taken from reference (Zhang, R., Shen, J., Xie, H. B., Chen, J., and Elm, J.: The role of organic acids
816 in new particle formation from methanesulfonic acid and methylamine, Atmos. Chem. Phys., 22, 2639-2650,
817 10.5194/acp-22-2639-2022, 2022b.)
818 [b] The value was taken from reference (Zhong, J., Li, H., Kumar, M., Liu, J., Liu, L., Zhang, X., Zeng, X. C., and
819 Francisco, J. S.: Mechanistic Insight into the Reaction of Organic Acids with SO$_3$ at the Air–Water Interface, Angew.
820 Chem. Int. Ed., 131, 8439-8443, 2019.)